Synthetic injectable and porous hydrogels for the formation of skeletal muscle fibers: Novel perspectives for the acellular repair of substantial volumetric muscle loss

Louise Griveau, Marion Bouvet, Emilie Christin, Cloé Paret, Lauriane Lecoq, Sylvie Radix, Thomas Laumonier, Jerome Sohier, Vincent Gache

Original Article

Journal of Tissue Engineering
Volume 15: 1–23

DOI: 10.1177/20417314241283148
journals.sagepub.com/home/tej
Sage

Synthetic injectable and porous hydrogels for the formation of skeletal muscle fibers: Novel perspectives for the acellular repair of substantial volumetric muscle loss

Louise Griveau[1], Marion Bouvet[1,2], Emilie Christin[2], Cloé Paret[2], Lauriane Lecoq[3], Sylvie Radix[4], Thomas Laumonier[5], Jerome Sohier[1*] and Vincent Gache[2*]

Abstract

In severe skeletal muscle damage, muscle tissue regeneration process has to face the loss of resident muscle stem cells (MuSCs) and the lack of connective tissue necessary to guide the regeneration process. Biocompatible and standardized 3D structures that can be injected to the muscle injury site, conforming to the defect shape while actively guiding the repair process, holds great promise for skeletal muscle tissue regeneration. In this study, we explore the use of an injectable and porous lysine dendrimer/polyethylene glycol (DGL/PEG) hydrogel as an acellular support for skeletal muscle regeneration. We adjusted the DGL/PEG composition to achieve a stiffness conducive to the attachment and proliferation of murine immortalized myoblasts and human primary muscle stems cells, sustaining the formation and maturation of muscle fibers *in vitro*. We then evaluated the potential of one selected "myogenic-porous hydrogel" as a supportive structure for muscle repair in a large *tibialis anterior* muscle defect in rats. This injectable and porous formulation filled the defect, promoting rapid cellularization with the presence of endothelial cells, macrophages, and myoblasts, thereby supporting neo-myogenesis more specifically at the interface between the wound edges and the hydrogel. The selected porous DGL/PEG hydrogel acted as a guiding scaffold at the periphery of the defect, facilitating the formation and anchorage of aligned muscle fibers 21 days after injury. Overall, our results indicate DGL/PEG porous injectable hydrogel potential to create a pro-regenerative environment for muscle cells after large skeletal muscle injuries, paving the way for acellular treatment in regenerative muscle medicine.

Keywords

Volumetric muscle loss, regenerative muscle medicine, injectable and porous hydrogels

Date received: 7 April 2024; accepted: 28 August 2024

[1]Laboratory of Tissue Biology and Therapeutic Engineering, CNRS, University of Lyon, Claude Bernard University Lyon 1, UMR5305 LBTI, Lyon, France
[2]Institut NeuroMyoGène, Unité Physiopathologie et Génétique du Neurone et du Muscle, INSERM U1513, CNRS UMR 5261, Université Claude Bernard Lyon 1, Univ Lyon, Lyon, France
[3]Molecular Microbiology and Structural Biochemistry, Labex Ecofect, UMR 5086 CNRS/Université de Lyon, Lyon, France
[4]Universite Claude Bernard Lyon 1, CNRS UMR 5246 Institut de Chimie et Biochimie Moléculaires et Supramoléculaires (ICBMS), COSSBA Team, Faculté de Pharmacie, ISPB, Lyon, France
[5]Department of Orthopedic Surgery & Department of Cell Physiology and Metabolism, Faculty of Medicine, Geneva, Switzerland

[*]These authors contributed equally to this work.

Corresponding authors:
Jerome Sohier, Laboratory of Tissue Biology and Therapeutic Engineering, CNRS, University of Lyon, Claude Bernard University Lyon 1, UMR5305 LBTI, 7 passage du vercors, Lyon 69007, France.
Email: Jerome.sohier@cnrs.fr

Vincent Gache, Institut NeuroMyoGène, Unité Physiopathologie et Génétique du Neurone et du Muscle, INSERM U1513, CNRS UMR 5261, Université Claude Bernard Lyon 1, University Lyon, 8 Avenue Rockefeller, Lyon 69008, France.
Email: Vincent.gache@inserm.fr

Graphical abstract

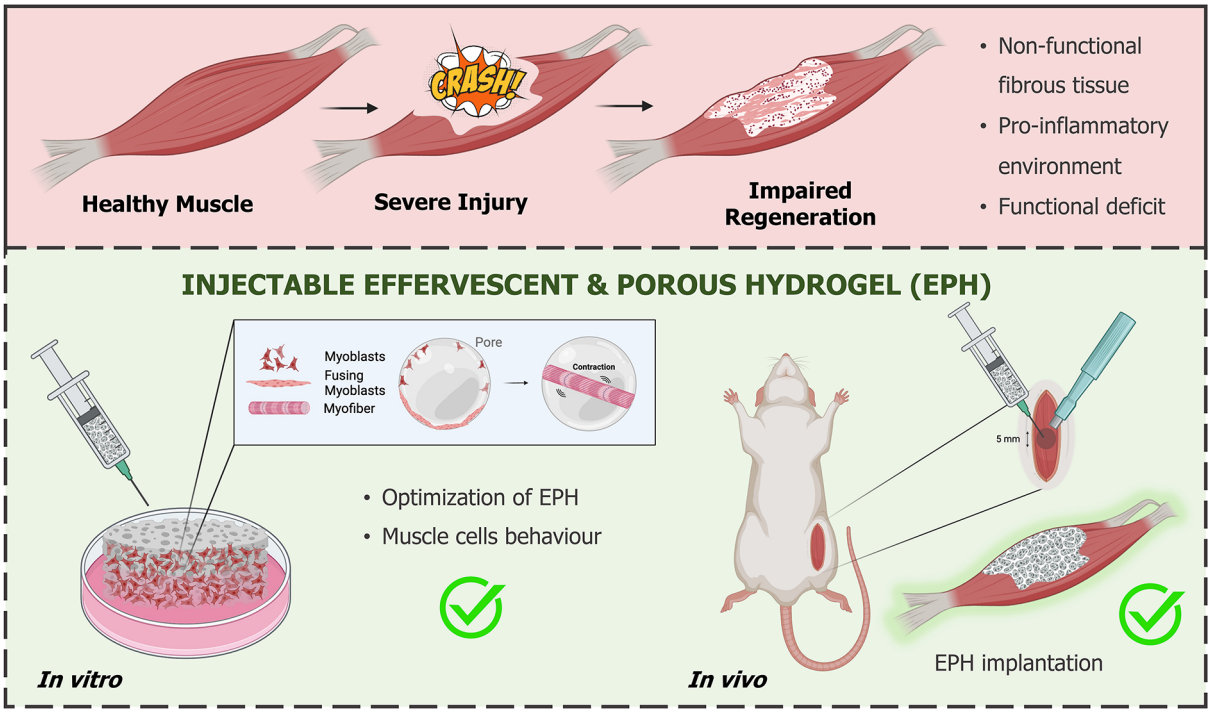

Introduction

Skeletal muscle constitutes the predominant tissue in the body, representing approximately 30%–45% of the total body mass.[1] Comprising post-mitotic muscle fibers formed through the fusion of specialized mononucleated myoblasts, skeletal muscles play a pivotal role in voluntary movements,[2] locomotion, thermoregulation, and substrate storage, particularly for amino acids.[3] Muscle tissue regeneration process is highly conserved in many species, including humans and rodent animals, and enables effective healing following minor traumas.[4] In such event, muscle stem cells (MuSC), dispersed throughout the entire muscle tissue exit their quiescent state to give rise to highly proliferative myoblasts, which fuse together to form new muscle fibers.[5] This efficient skeletal muscle tissue healing process involves a well-coordinated series of events leading to the complete restoration of normal tissue architecture and functions. However, in cases of significant muscle injuries, such as volumetric muscle loss (VML), this repair process is hindered. The tissue's original functionality, especially contractility, remains unrecovered due to the ineffective remodeling process.[6] The absence of an orderly reconstitution of a structurally and mechanically suitable extracellular matrix (ECM), and the concomitant ablation of resident MuSC results in a non-functional disabling fibrotic scarring.[7] In addition, recent studies underline the role of chronic inflammation linked with severe muscle injuries, hindering the reparative contribution of MuSC and promoting fibrosis.[8] To date, therapeutic options are extremely limited,[9] mostly relying on muscle autografts/flaps[10] to close wounds, offering limited success in fully restoring muscle function and the ability to contract.[11,12]

Regenerative medicine strategies, aiming to enhance the functional repair of damaged tissues using biomaterial supports, hold great promise for treating, severe muscle injuries and VML.[13,14] However, existing cellular or acellular biomaterial-based approaches have not yet achieved successful repair clinically.[15] Effective strategies must overcome physiological constraints: (i) connect the adapted biomaterial to the remaining injured tissue, (ii) replace the missing connective tissues to provide support for cells and guide them toward muscle regeneration (iii) mediate the inflammatory response to promote myogenic muscle cells and limit fibroblast colonization.

Therefore, such biocompatible and standardized 3D biomaterials should be injectable into the injured muscle to ensure ease of use and to intricately delineate and conform to the defect shape. Indeed, a tight interaction between biomaterials and wound edges would ideally facilitate the local recruitment of remaining resident MuSC from the non-injured tissue. The presence of porosity is of critical importance to allow cell infiltration, vascular and nerve ingrowth over large volumes.[16] The design of standardized porosities and 3D architectures have thus been explored *in vitro*, with efforts to recapitulate the topographical cues found in the native skeletal muscle tissue, strategically guiding the

muscle repair process.[17–21] The design of both injectable and porous biomaterials for tissue repair remains scarce but have demonstrated considerable potential,[22] and starts to be explored in the context of skeletal muscle injuries.[23]

The ideal biomaterial should provide a biophysical and biochemical environment incentive for muscle fibers formation and maturation. In the last decades, it has become clear that the microenvironment is a key regulator of muscle cell behavior during the process of myogenesis through mechano-physical, biochemical, and architectural cues.[24] Furthermore, to ensure cell survival, tissue formation, and long-term functionality of the repaired muscle, the biomaterial should support neo-angiogenesis and allow an efficient innervation, particularly for VML of complex and large sizes.[25] Considering that there is no clinically approved therapy for the treatment of large muscle defects or extreme damages, we investigated an injectable and porous hydrogel, with specific myogenic bioactivity, for its ability to create a pro-regenerative environment for cells after large skeletal muscle injuries.

The DGL/PEG hydrogel is biocompatible, and exhibits broad mechanical properties versatility while conveniently interacting with fibroblasts by means of polycationic charges brought by the DGL amines.[26] We have recently developed a swift and straightforward injectable delivery of this innovative hydrogel that allows a tight interaction with surrounding tissues while ensuring the creation of an adequate porosity for cellular infiltration and vascularization.[22] The method relies on a controlled effervescent reaction performed concomitantly with the injection of hydrogel precursors. The crosslinking process, occurring simultaneously with the effervescent reaction, entraps the CO_2 bubbles generated, forming an interconnected porosity. The nontoxic nature of effervescence along with its ability to preserve the biochemical integrity of proteins, makes it suitable for in situ formation of a 3D structure within the hydrogel. These effervescent-porous hydrogels showed promising results in contact with fibroblasts and extensive vascularization potential when subcutaneously injected in mice, highlighting their *in vivo* potential.

Hence, this study adapted the DGL/PEG hydrogel mechanical and biochemical aspects of scaffold design (stiffness and composition) to support *in vitro* the attachment and proliferation of muscle cells while sustaining the formation/maturation of muscle fibers. To achieve this, non-porous DGL/PEG hydrogels with varying stiffness and DGL:PEG ratios were synthetized, and the behavior of murine immortalized myoblasts cells was evaluated to determine the optimal myogenic environments (combination of myoblasts spreading, proliferation, velocity, and differentiation). We next evaluated the compatibility with human myoblasts differentiation within the effervescently generated 3D porous environment to select the best composition for promoting efficient myogenesis. Finally, this "myogenic-hydrogel" was tested for its regenerative potential into large muscle defects in the *tibialis anterior* of rats over 21 days regarding cellularization and its contribution to muscle repair. Our results highlight that our acellular strategy sustains the attachment of the remaining injured tissue with the porous DGL/PEG hydrogel and acts as a guiding scaffold at the periphery of the defect to facilitate the formation and anchorage of a neo-regenerated area containing aligned muscle fiber bundles.

Materials and methods

A 2D flat hydrogel preparation

Poly(L-lysine) dendrimers of third generation (DGL; molecular weight of 22000 g/mol, Colcom, France) and Poly(ethylene glycol; PEG)-bis(*N*-succinimidyl succinate; PEG-NHS, 2000 g/mol, Sigma Aldrich) were solubilized at 400 mg/mL in phosphate buffered saline (PBS, Euromedex) and DMSO (Sigma Aldrich), respectively, before use. Stock solutions of PEG-NHS in DMSO and DGL in PBS (400 mg/mL) were added to the adjusted volume of PBS to obtain the desired concentrations (i.e. 1/25, 1.6/25, 2/19, 2/25, 2/37, and 2/50 mM DGL/PEG) in 2 mL conical tubes (Maxymum Recovery, Axygen) followed by vigorous homogenization. To form cylinders, 400 µL of hydrogel precursors were allowed to crosslink inside the tubes to then be retrieved and sectioned using a vibratome (7550 Integraslice) at a 50 Hz frequency, 1 µm amplitude, and a slow blade speed of 0.10–0.15 mm/s to obtain hydrogel discs of 2 mm high and 9.1 mm wide. For hydrogels adhered in well plates, 90 µL of mixed liquid hydrogel precursors were rapidly deposited in wells of a 48 well plate and quickly recovered with 600 µL of hydrated butan-1-ol for meniscus smoothing. After crosslinking, hydrogels were extensively washed and sterilized overnight in an EtOH/PBS (70/30; v/v) solution at 4°C followed by extensive washing with sterile DPBS. Hydrogels were kept immersed in sterile DPBS at 4°C before use. Hydrogel discs were 1 cm wide, covering the entire diameter of the well and were 0.7 mm thick to preclude the possibility that cultured cells sense the stiffness of the underlying plastic dish. The 2D flat hydrogels were referred as hydrogels without the macroporous architecture.

A 2D flat hydrogel characterization

Fourier transform infrared spectroscopy (FT-IR). The structure of PEG (400 mg/mL in DMSO), DGL (400 mg/mL in pure water), and of a 2/25 mM DGL/PEG hydrogel (prepared in pure water instead of PBS and freeze-dried prior analysis), were analyzed by FT-IR using a PerkinElmer Spectrum Two FT-IR spectrometer equipped with a universal attenuated total reflectance. The infrared spectra were scanned in the range of 4000–450 cm^{-1} and the number of scans was 4.

Nuclear magnetic resonance (NMR). A 2/25 mM DGL/PEG hydrogel was prepared directly in a thin-wall 3.2 mm NMR rotor, followed by ultracentrifugation (30 min at 100,000*g*, 25°C) using an NMR filling tool. Before closing the rotor, 1.5 µl of 4,4-dimethyl-4-silapentane-1-sulfonic acid (DSS Sigma Aldrich) were added for NMR chemical shift referencing. Solid-state NMR experiments were recorded using a 3.2 mm triple-resonance (^{1}H, ^{13}C, and ^{15}N) probe head at static magnetic field of 800 MHz proton resonance frequency (Bruker Avance II) and set-up in ^{1}H and ^{13}C double mode, at a 17.5 kHz magic-angle spinning (MAS) spinning frequency and at a temperature of 25°C. The radio-frequency field strengths for ^{13}C and ^{1}H were set to 50 and 100 kHz, respectively. Since the hydrogel gave no signal in CP (cross-polarization) experiments, an INEPT (insensitive nuclei enhanced by polarization transfer) experiment was performed instead. A 2D ^{1}H-^{13}C-INEPT spectrum was recorded with 48 scans over 8 h detected in the carbon dimension.

For reference solution NMR spectra, solutions of DGL and PEG-NHS were prepared at 2 mM in DMSO-d_6 (Carlo Erba) and at 25 mM in D_2O (Eurisotop), respectively. A ^{1}H-^{13}C HSQC spectra were recorded on a 600 cMHz spectrometer equipped with a cryo-probe, at 25°C and for 30 min, with a spectral width in carbon dimension of 70 ppm. A HH-TOCSY was also recorded on PEG-NHS for 30 min with a mixing time of 80 ms and with a spectral width in proton dimension of 15 ppm.

A ^{1}H and ^{13}C chemical shifts of PEG-NHS and PEG-DGL were predicted using MestReNova software (Mestrelab) to assist in resonance assignment.

A ^{1}H and ^{13}C NMR chemical shifts of PEG-NHS in solution (see Supplemental Figure S1B for nomenclature): δ_{C1}=72.3 ppm; δ_{H1}=3.75 ppm; δ_{C2}=72.3 ppm; δ_{H2}=3.50 ppm; δ_{C3}=41.9 ppm; δ_{H3}=3.30 ppm, δ_{C4}=32.4 ppm; δ_{H4}=2.56 ppm, δ_{C5}=29.1 ppm; δ_{H5}=2.96 ppm, δ_{C6}=31.2 ppm; and δ_{H6}=2.73 ppm.

Mechanical properties. For mechanical testing, 400 µl of hydrogels of various concentrations (1/25, 1.6/25, 2/19, 2/25, 2/37, and 2/50 mM DGL/PEG) were formulated as described above. The mechanical properties of non-porous hydrogel cylinders (2 mm × 9.1 mm) of various compositions were analyzed by cyclic compression with a dynamic mechanical analyzer (DMA 242 E Artemis, NETZSCH, Germany). Hydrogels domain of linearity was first determined with a strain sweep test in compression performed in PBS immersion at room temperature. Samples were then subjected to compression at 10% constrain, 50 µm amplitude, and 1 Hz frequency in PBS immersion at room temperature. The elastic and the loss of hydrogels were reported.

Swelling ratio. The swelling ratio (Q_s) of 2 mm thick and 9 mm wide half circle hydrogels was determined in PBS at 37°C from non-porous hydrogels. Briefly, hydrogels were immersed in nitrogen and freeze-dried for 48 h at 400 mTorr. Freeze-dried samples were weighted using an analytical balance, immersed in a 37°C PBS solution and kept at 37°C. Samples were weighted after 1, 2, 4, 8, 24, and 48 h of immersion.

Measurements were taken until reaching equilibrium. The swelling ratio was calculated using the following equation:

$$Q\mathrm{s} = \frac{W_\mathrm{s} - W_\mathrm{d}}{W_\mathrm{d}}$$

where W_s represents the swollen weight of the sample at time t and W_d represents the dry weight of the freeze-dried sample.

Injectable and porous hydrogels formulation

Effervescent porous DGL/PEG hydrogels (EPH) were prepared as described elsewhere.[22] Briefly, DGL at desired concentration and potassium carbonate (P_c at 0.477 M in distilled water) were mixed in PBS, vigorously homogenized, heated at 37°C, and transferred into the first cartridge of a dual-chamber syringe (Adhesive dispensing Ltd, UK). Concomitantly, a surfactant, the pluronic® F-68 at 3.3%, glacial acetic acid (Gaa at 0.635 M), and PEG-NHS in dimethyl sulfoxide (DMSO, Sigma-Aldrich) at desired concentration were mixed, homogenized, and placed in the second cartridge of the dual-chamber syringe. Both compartments of the dual-chamber syringe were balanced to obtain a final volume of 400 µL at a ratio 1:1. Solutions were then injected through a static mixing nozzle (adhesive dispensing Ltd, UK) inside conic tubes, with the concentration reported being the final concentration in the vial. After crosslinking, hydrogels were removed and manually cut to obtain cylinders of 2 mm high. EPH cylinders were then sterilized overnight in EtOH/PBS (70/30; v/v) solutions at 4°C followed by an extensive washing with sterile DPBS. They were kept immersed in sterile DPBS at 4°C prior use. Various hydrogel conditions (1.6/25, 2/25, and 2/37 mM DGL/PEG) were studied with a set Gaa:Pc molar ratio (1.33:1), Gaa/Pc concentration (1.1 M), and surfactant concentration (3.3%).

Cell culture

Mouse skeletal myoblasts cells (C2C12 cell line, DSHB) were grown in Dubecco's Modified Eagle Medium (DMEM, Gibco) 1× supplemented with 15% fetal bovine serum (FBS) and 1% penicillin/streptomycin (Sigma Aldrich) until reaching 80% confluence. When required, cells were switched to DMEM containing 2% horse serum (Gibco, Thermofisher scientific) for 6 days to induce myogenic differentiation. Primary human myoblasts (pHMs) were kindly provided by the department of orthopedic surgery, Geneva university hospitals & faculty of medicine.[27]

Isolated pHMs were grown in Ham's F10 medium supplemented with 15% FBS; 0.5 mg/mL bovine serum albumin (BSA); 0.5 mg/mL fetuin; 0.39 µg/mL dexamethasone; 0.04 mg/mL insulin, 1 mM creatine; 100 µg/mL pyruvate; 50 µg/mL uridine (Sigma Aldrich); and 5 µg/mL Gentamycin (Gibco) and refreshed every second day. Cells were induced in differentiation by using a DMEM 1× medium supplemented with 0.5 mg/mL BSA; 0.01 mg/mL insulin; 1 mM creatine; 100 µg/mL pyruvate; 50 µg/mL uridine; and 10 µg/mL Gentamycin. All cell types were maintained in a humid incubator at 37°C and in 5% CO_2.

Cell seeding on coatings. Wells of 24 well plates were coated by passive adsorption with 1 mg/mL DGL, in DPBS for 4 h at 4°C followed by extensive washing with DPBS prior use. When performing coatings, bare polystyrene wells were used as positive controls. Matrigel (Corning) was also used as a positive control for muscle cells. Matrigel at 1/100 in growth medium was added to the well and let to polymerize for at least 30 min at RT before washing with warm DPBS.

C2C12 cells were seeded on DGL and Matrigel coatings and on plastic dish at 4000 and 40,000 cells/cm². Cells seeded at 40,000 cell/cm² were grown for 24 h before inducing their differentiation and fusion. Briefly, wells were washed once with warm DPBS and immersed in serum-depleted medium for 6 days.

Cell seeding on 2D flat hydrogels of various composition. Sterilized 2D hydrogel layers formulated on 48 well plates were soaked in growth medium and kept at 37°C, 30 min before cell seeding. C2C12 cells, 15,000 cells/specimen, were seeded on 2D hydrogels of various concentration in 0.6 mL culture medium. Cells were grown for 4–6 days before inducing their differentiation when reaching 80% confluence using protocol described above.

Cell culture onto 3D porous hydrogels of various composition. Sterilized 2-mm high EPH were soaked in growth medium and kept at 37°C, 30 min before cell seeding. C2C12 cells (20,000 cells/specimen) and pHMs (60,000 cells/specimen) were deposited on the top of EPH of various concentrations in 100 µL of culture medium. Samples were incubated at 37°C for 2 h to allow for cell attachment before adding 0.6 mL of growth medium to each well. Cells were grown for 4–8 days before depleting the medium in serum for 6–14 days.

At dedicated time points after the inducement of differentiation, cells on coating, 2D hydrogels, or into 3D EPH were fixed for 20 min at 37°C in a mix of sucrose 4% and paraformaldehyde (PFA, Thermofisher scientific) 4% followed by three washing in PBS. Specimens were stored immersed in PBS at 4°C prior use.

Metabolic activity measurements. Cells metabolic activity was measured with an alamar® blue assay on C2C12 cells seeded at 4000 cells/cm² on surfaces coated with DGL, and matrigel or on bare polystyrene (crude plastic) after 24, 48, and 120 h in growth medium.

Briefly, the culture medium was removed from all conditions, cells were washed with warm and sterile DPBS and 400 µL of a 10% alamar® blue mix in complete culture medium was added onto the cells. After 3 h of incubation at 37°C and 5% CO_2, the supernatants were harvested and their fluorescence measured with a fluorescence microplate reader (TECAN infinite® 200) at excitation 535 nm and emission 610 nm. C2C12 seeded at increasing densities without any treatments were used as positive controls for standard curve linearity assessment to determine the range in which alamar® blue assay could be conducted. Data are presented normalized to the data obtained on crude plastic.

Cell migration and morphology by time Lapse. To study C2C12 cells in proliferative conditions, they were seeded on 2D hydrogels as described above and tracked by time-lapse videos. Briefly, 7 h after seeding, plates were transferred into a time-lapse microscope (Zeiss Axio Observer Z1 inverted) at 37°C and 5% CO_2. Five bright field pictures per well were taken using a 10× lens (N-Achroplan 0.25 ph1, N.A 0.25) every 10 min for 24 h to follow cellular movement and morphology over time.

Cellular velocity (from 7 to 30 h post-seeding), confluence (7-, 24-, and 30-h post-seeding), and morphology (30 h post-seeding) were assessed by image analysis of time-lapse video using ImageJ.

In vitro immunofluorescence staining and image analyses

EPH cylinders were either used whole in immersion or cut in slices. EPH slices were obtained by first embedding fixed samples in optimal cutting temperature solution (OCT) by successive baths of increasing concentrations: 20%, 50%, 80%, 90%, and 100% in PBS for 30 min each. EPH were then cut (16–30 µm) with a cryotome (Leica C3050S), deposited on glass slides (Superfrost plus, thermofisher scientific), and fixed with acetone for 20 min at −20°C.

Cells on coatings, 2D hydrogels, or into 3D EPH were permeabilized with a 0.1% triton X-100 (Euromedex) solution in PBS followed by an immersion in blocking solution (5% BSA in PBS) for 1 h. A C2C12 and pHMs undifferentiated and differentiated phenotypes were evaluated by a staining with antibody directed against Myosin Heavy chain (MyHC, MF-20 1:10, DSHB, and clone MF20). pHMs cell morphology, cytoskeleton organization and protein expression were detected through

Table 1. Primer sequences used for real time PCR.

Genes	Primers	Sequence
MyH4-Myosin Heavy Chain 4	Forward	CAA-GTC-ATC-GGT-GTT-TGT-GG
	Reverse	TGT-CGT-ACT-TGG-GAG-GGT-TC
Glyceraldehyde 3-phosphate dehydrogenase (GAPDH)	Forward	AAC-TTT-GGC-ATT-GTG-GAA-GG
	Reverse	ACA-CAT-TGG-GGG-TAG-GAA-CA
RPl41A-60S ribosomal protein L41-A	Forward	GCC-ATG-AGA-GCG-AAG-TGG
	Reverse	CTC-CTG-CAG-GCG-TCG-TAG

immunofluorescence analysis after incubation with desmin Y66 (1:50, Abcam ab32362), and sarcomeric alpha-actinin (1:500, Sigma Aldrich A7811). Samples were incubated with monoclonal antibodies in a solution of BSA 1% for 2 h. Secondary antibodies (Alexa Fluor 647—1/500 or Alexa fluor 555 1/500 from Thermofisher) were then applied on samples for 2 h in a wet chamber. For nucleus and actin staining, 4,6-diamidino-2-phenylindole (DAPI, Sigma Aldrich) at 2 µg/mL and Alexa fluor 488-conjugated phalloidin (Invitrogen) at 4 µg/mL were added for 10 min. All incubations steps were performed at room temperature, samples were rinsed three times in PBS between each step and kept immersed at 4°C in PBS prior use.

For 2D hydrogels, three mosaics of 12 pictures were performed for each condition. Samples on glass slides were mounted with fluoromount and whole EPH were kept immersed in PBS 1× to be analyzed with an upright laser scanning confocal microscope (LSCM—Zeiss Imager.Z2). On EPH, 100 µm stacks were realized on five various positions and orthogonally projected. Formation of skeletal muscle cells (myotubes) was appreciated with myosin heavy chain (MyHC), desmin, and alpha-actinin antibody staining. The number of nuclei per myotubes and myotubes area, width (average of three distinct positions in the myotube), and length (feret diameter) were determined by image analysis with ImageJ. The elongation index was calculated as the ratio of myotubes Feret's diameter on their width. The fusion index was calculated as the number of nuclei inside MyHC+ structure on the total number of nuclei. For myotube morphology quantification, myotubes of at least two nuclei were measured and at least three samples per condition were analyzed at three various cell passages. Between 80 and 211 myotubes were analyzed per condition.

Determination of myogenic differentiation by real time PCR

To quantitatively measure the expression levels of Myh4, real-time polymerase chain reaction (RT-PCR) was performed on 3D EPHs after 1, 3, and 6 days in serum-depleted medium. For every condition at least three EPHs were harvested and frozen in liquid nitrogen. Frozen samples were deposited into 2.0 mL lyzing Matrix tubes containing 1.4 mm ceramic spheres and subjected to high-speed lysis with FastPrep-24 5G Instrument. Total RNA was isolated from the supernatant of lyzed 3D scaffolds using TRIzol® reagent according to the manufacturer's recommendations. The purity and concentration of the isolated RNA were measured by a spectrophotometer (Nanodrop 2000 ThermoScientific). A Single-stranded cDNA synthesis was performed with 500 ng total RNA using the GoScript™ Reverse Transcription System Kit from Promega following the manufacturer's recommendations. Quantitative polymerase chain reaction (qPCR) of transcripts and endogenous controls, GAPDH and RPl41A-60S, was performed using SYBR® Green Supermix in a CFX Real-Time PCR Detection System (Bio-Rad, Hercules, CA). Thermal cycle conditions were an initial 95°C for 10 min followed by 40 cycles at 95°C for 10 s and 60°C for 30 s.

Data were analyzed using the E^{-Ct} method with normalization to Ct of housekeeping genes GAPDH (glyceraldehyde 3-phosphate dehydrogenase) and ribosomal protein L41-A. To determine relative expression of muscle markers, primers were designed to explore the various phases of myogenesis. Primer sequences are described in Table 1.

In vivo characterization of EPH

Experimental design. Male Sprague Dawley rats (Janvier Labs, Le Genest-Saint-Isle, France, 14-week-olds were divided into two groups (n=3 per group) that each received a VML injury: (1) left empty, (2) injected with EPH; for 7, 14, and 21 days. Animals were anesthetized by intraperitoneal injection of ketamine (50 mg/kg) and xylazine (6 mg/kg). Core temperature was maintained using the surgical bed at 40°C. Rats were administered buprenorphine (0.05 mg/kg, subcutaneously) 45 min before and 6 h after the surgery, and each 24 h thereafter for the first 48 h post-surgery. Animal pain and distress were assessed daily for the first week post-surgery to determine the need for any additional analgesia; no animal required additional analgesia after the first 24 h post-surgery. All animals were euthanized under isoflurane anesthesia and decapitation. All the experiments and procedures were conducted in accordance with the guidelines of the local animal ethics committee of the University Claude Bernard—Lyon 1 and in accordance with French and European legislation on animal experimentation and approved by the ethics committee CECCAPP and the French ministry of research (*APAFIS#34145-2021111918561554v2*).

Muscle defect model and EPH injection. The surgical procedure for creating VML in the rat TA muscle was adapted from a previously described procedure.[28] Once deeply anesthetized, the rats were shaved, and a skin incision was made distally at 32 mm from the distal origin of the TA muscle (foot) to 42 mm of the proximal origin of TA (knee). The skin was separated from the connective tissue (muscle fascia) by blunt dissection. A longitudinal incision was made along the fascia, which was then gently separated from the TA muscle, taking care to keep it intact for later repair. With the TA exposed, a 5 mm-biopsy punch was used to create the full-thickness defect. The punch was inserted until reaching the tibia underneath. The muscle was excised with scissors and the excised defect was then blotted and weighed. The average weight of the excised muscle was 110 mg, which corresponds to 15% of the muscle weight.

Immediately after creation of the muscle defect, a 2/37 mM DGL/PEG EPH was injected into the defect at a volume of 260 µl by connecting the static mixer to a 21 G needle. After crosslinking (10 s), the porous hydrogel in excess was trimmed with scissors and the fascia and skin were stitched up using silk suture 9-0 and 6-0, respectively.

Tissue harvest, histology, immuno-histochemistry, and immunofluorescence. TA muscles were dissected, weighed, and fixed with PFA 4% + sucrose 4% during 4 days at 4°C. After extensive PBS rinse, muscles were embedded with paraffin using a tissue processor (HISTOS 5, Milestone), and stored at room temperature until sectioning. Using a Leica RM2245 microtome, samples were cut into 5 µm-thick sections and mounted on slides. After dewaxing, samples were stained with Hematoxylin and Eosin and Masson's Trichrome using standard procedure.

For immuno-histochemistry, paraffin-embedded 5 µm-sections were dewaxed, and antigenic site retrieval was carried out by microwaving for 20 min in Tris 10 mM-EDTA 1 mM (pH9). The samples were then incubated with the primary antibody (MyoD, Fisher Scientific, 18943-1-AP) overnight at 4°C. Having blocked endogenous peroxidase activity with 0.5% hydrogen peroxide, samples were incubated with the secondary antibody for 45 min at room temperature (Envision Rabbit, Dako, ref. K4003). Antigen-antibody complexes were revealed by tetrahydrochloride diaminobenzidine (DAB, Dako, K3468) and cells were slightly counterstained with Mayer's hematoxylin. Sections were mounted with aqueous medium for microscope observation. A section was also incubated with PBS-BSA 3% as negative control.

For immunofluorescence, paraffin-embedded 5 µm-sections were dewaxed, and antigenic site retrieval was carried out by microwaving for 20 min in 10 mM citrate buffer (pH6) for CD11 and CD 206 staining or by hyaluronidase 0.5% (1 h at room temperature) for Type IV Collagen. The samples were incubated with primary antibodies (rabbit monoclonal anti-CD11c, Abcam, ab219799, 1/10; rabbit anti-mouse Type IV Collagen, 1/50, 20451-435b, Novotec) overnight at 4°C. After washing in PBS, samples were incubated for 1 h at room temperature with the corresponding secondary antibody (rabbit alexafluor 488 or 568, 1:1000, Thermofisher). For CD206, after a new washing in PBS, the samples were incubated with the primary antibody (anti-CD206, Abcam, ab300621, 1/200) overnight at 4°C, followed by incubation with the secondary antibody (Rabbit Alexafluor 568) for 1 h at room temperature. Sections were mounted with aqueous medium with DAPI (Invitrogen) for fluorescent microscope observation. A section was also incubated with PBS-BSA 3% as negative control.

Alternatively, samples were embedded with 3% low melting agarose (Invitrogen). Abour 150 µm sections were then cut using a vibratome (VT100 S, Leica). Tissue sections were permeabilized using 0.1% TritonX-100 in PBS for 20 min at room temperature. To prevent non-specific binding of antibodies, sections were blocked using 5% goat serum and 2% bovine serum albumin (Euromedex) in PBS for 1 h at room temperature. Wheat Germ Agglutinin (Invitrogen, 1:1000) was diluted in blocking solution applied to the sections and incubated for 1 h at room temperature. After three washes with PBS, sections were incubated for 15 min with DAPI (1:100, Sigma-Aldrich) at room temperature. For sarcomeric myosin (MF20: 1:3, DSHB), after blocking, sections were incubated in primary antibody solutions overnight at 4°C. They were then washed in PBS and incubated in rabbit Alexafluor 488, 555, or 647 labeled secondary antibodies (1:1000, Thermofisher) at room temperature for 1 h, prior to be stained with DAPI for 15 min. All sections were finally washed twice with PBS before being mounted with Fluoromount® mounting medium (Thermofisher). Stained slides were stored at 4°C in the dark until imaging.

Imaging and image analysis

Imaging. Stained sections were imaged using either a Zeiss AxioImager 7 slide scanner or a Nikon AXR, equipped with 10× and 20× air objectives. Tile-stitched was made to view the entire longitudinal area of each section.

Quantitative analysis. ImageJ software was used for quantitative analysis of all images.[29] The "polygon tool" within ImageJ enabled precise delineation and measurement of the areas occupied by both muscle tissue and the EPH scaffold, as well as the pore size within the images. This approach allowed accurate determination of the spatial distribution and coverage of the EPH implant within the muscle tissue.

Analysis of pore structure. Using data on the surface area covered by the EPH structure and the number of pores counted, along with their individual surface areas, the percentage of closed pores was calculated. "Closed pores" refer to the distinct void spaces within the EPH scaffold that are visibly sealed as observed in the acquired images. Additionally, the percentage of empty pores was assessed to monitor the degree of cellular infiltration and scaffold remodeling over time.

Myofiber alignment assessment. We carefully measured the percentage of myofibers that were aligned versus non-aligned at 7 and 21 days after muscle injury, with and without EPH injection. First, using the "Oval" selection tool in ImageJ, an area encompassing the injured muscle, including the visible granulation tissue, was delineated on every image. This oval area was then duplicated by drawing a second oval shape, twice its size, around the initial one, effectively defining the immediate healthy/injured-muscle interface. This region comprised the EPH implant (if present), the granulation tissue, and the adjacent untouched muscle tissue. Subsequently, within this cropped area, myofiber regions around the lesion were visually identified and separated into two categories: aligned and non-aligned. The areas occupied by each zone were quantified, and each area was attributed to the corresponding category of aligned or non-aligned myofibers. Finally, the percentages of aligned and non-aligned myofibers were calculated, leading to the generation of cumulative histograms representing the myofiber distribution, categorized into aligned and non-aligned, for each condition.

EPH degradation rate assessment. To study the degradation rate of the injected EPH over the implantation period, serial longitudinal cross-sections of the muscle samples (5 µm-thick) were prepared at 7- and 21-day post-implantation. Various levels of cross-sections were selected from the rats' TA muscle to quantify the percentage of EPH visible in Masson's Trichrome-stained images relative to the total muscle tissue in each section. The use of different levels of slices from the muscle ensures a comprehensive analysis of the EPH degradation, capturing variations across the entire muscle tissue.

Statistical analysis

Statistical analyses were performed with Graphpad prism. Tests were performed using variance analysis (ANOVA) or *t*-test after a Shapiro-Wilk normality test. *In vitro* graphical data are shown as mean ± standard deviation (SD) and *p*-values of 0.05 and below were considered significant. *In vivo* data values are presented as mean ± standard error (SE).

Results

Determination of DGL/PEG hydrogel stiffness and composition

We synthetized hydrogel by the chemical crosslinking between poly(ethylene) glycol (PEG) and lysine dendrimers (DGL) though *N*-hydroxysuccinimide (NHS) coupling chemistry (Figure 1(a) and (b)). The crosslinking was achieved by simply mixing both components in aqueous solution at adequate concentrations and ratios followed by vigorous homogenization. The PEG molecules functionalized with NHS activated esters at both molecule ends react with the primary amines (NH_2) present in high densities on the DGL surface to form covalent amide bonds. The dual reactive functionality of NHS-PEG-NHS toward DGL leads to the formation of a polymer network. Characterizations of reactants and resulting DGL/PEG hydrogels by FT-IR and RMN (Figure S1) indeed indicate such a polymerization reaction. The FT-IR spectra of PEG-NHS, DGL, and DGL/PEG hydrogel (Supplemental Figure S1A) show the characteristic stretching vibrational bands as sp^3 C–H (CH_2 groups) at 2871 cm^{-1}, C–O stretching vibration at 1250, 1200, and 1098 cm^{-1} corresponding to ether groups in the PEG molecule[30,31] and DGL/PEG hydrogel. Regarding DGL, the absorption band at 1550 cm^{-1} could be attributed to $\nu_{C\text{-}N}$ of polylysine chains.[32–35] The molecule displayed characteristic C–N stretch peaks of aliphatic amines at 1200 and 1140 cm^{-1}. The secondary amides present in the DGL can be inferred through the two strong absorbance bands at 1639 and 1667 cm^{-1}, which are characteristic of the C=O stretch of secondary amide. In the DGL/PEG hydrogel spectrum, both PEG and DGL profiles can be recognized. However, it is important to notice the disappearance of the absorption at 1738 cm^{-1}, which can be ascribed to the C=O bonds of *N*-hydroxysuccinimide moieties present at both ends of the PEG molecule, in the DGL/PEG hydrogel spectrum. Further indicating that the PEG-NHS molecules reacted with the amine present on the DGL during crosslinking, the characteristic secondary amide peak at 1667 and 1639 cm^{-1} and companion peak at 1542 cm^{-1}, corresponding to the N-H bend of the secondary amide group, are more intense. The water present in the hydrogel is clearly visible by the absorption peak at 3400–3200 cm^{-1}, belonging to the stretching of the –OH group, and the peak at 1639 cm^{-1}, caused by the bending vibration of O-H.

The presence of both PEG and DGL in the formed hydrogel was confirmed by solid-state NMR, as shown in the ^{1}H-^{13}C INEPT NMR spectrum in Supplemental Figure S1B. Solution NMR reference ^{1}H-^{13}C spectra of DGL and PEG-NHS were recorded for comparison. For DGL, the resonances obtained are characteristic of the ^{1}H chemical shifts reported in the literature for polylysine[36] and for third generation lysine dendrigrafts.[37,38] PEG resonances

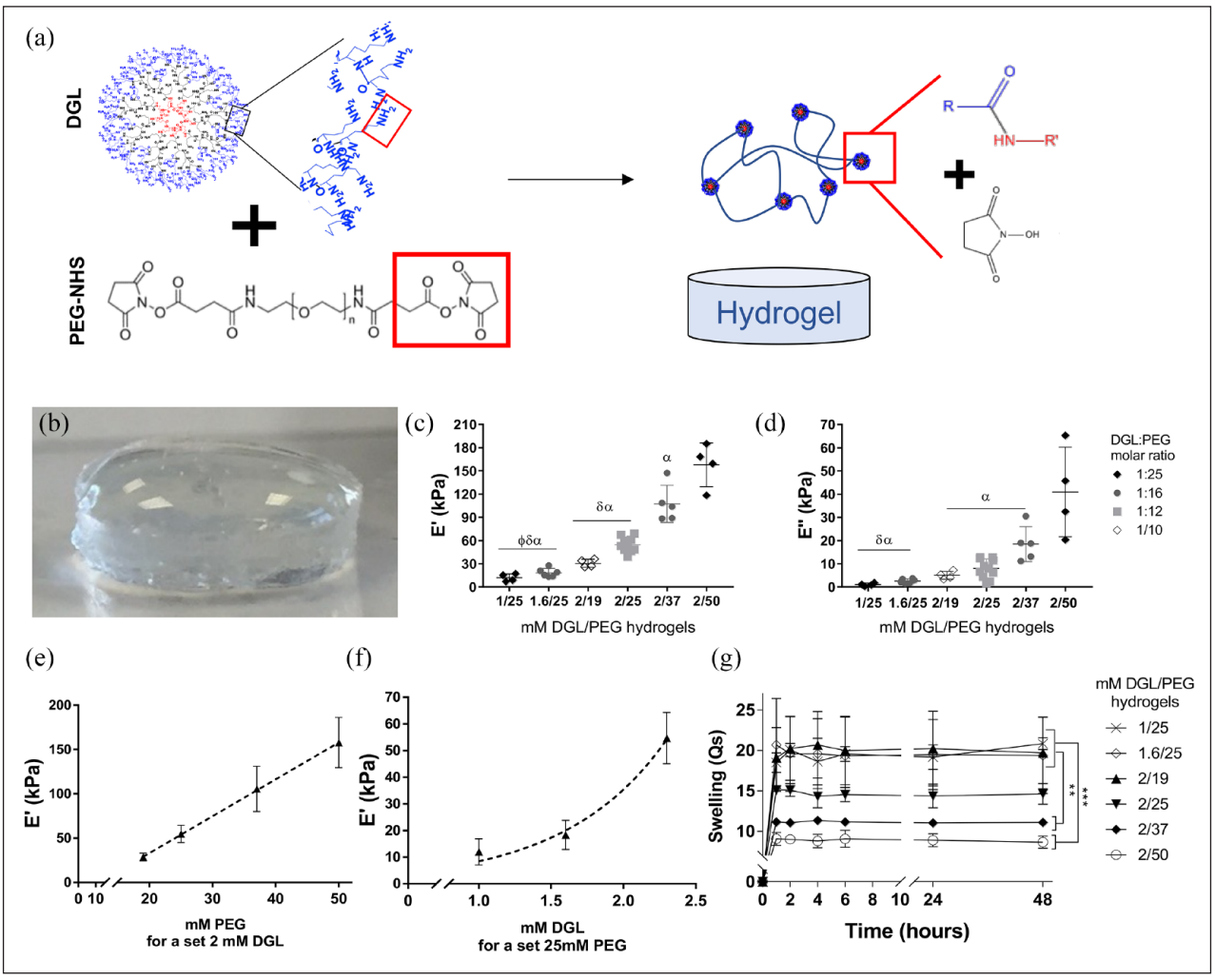

Figure 1. DGL/PEG hydrogel formulation and mechanical characterization: (a) Illustration of the chemical reaction occurring between DGL and PEG-NHS to form cross-linked DGL/PEG hydrogel and (b) representative picture of a 2/25 mM DGL/PEG hydrogel disc of 2 mm thickness and 9.1 mm diameter at room temperature. (c) Elastic modulus (E') and (d) loss modulus (E''), in compression of DGL/PEG hydrogels of various concentration and ratio (kPa). (e) Elastic modulus as a function of DGL/PEG concentration for a set DGL concentration (2 mM) and (f) for a set PEG concentration (25 mM) Lines: (e) linear (R^2: 0.9998) and (f) exponential (R^2: 0.8702) regression. (g) Swelling ratio over time of hydrogels of various DGL/PEG concentration (mM). (c and d) One-way ANOVA + Tukey's multiple comparison test $p < 0.05$ compared to Φ: 2/25, δ: 2/37, α: 2/50 mM DGL/PEG hydrogel. G: One-way ANOVA + Tukey's multiple comparison test *$p < 0.05$. **$p < 0.01$. ***$p < 0.001$.

can be identified based on known chemical shifts described in the literature[39] and using MestReNova software predictions for ^{1}H and ^{13}C chemical shifts. The DGL signals overlapped well between solution NMR and solid-state NMR of the hydrogel (Supplemental Figure S1B). Conversely, some PEG-NHS signals displayed discrepancies. While the methylene groups (1), (2), and (3) were mostly unaffected (δ_{C1} = 72.3 ppm; δ_{H1} = 3.70 ppm; δ_{C2} = 71.5 ppm; δ_{H2} = 3.62 ppm; δ_{C3} = 41.8 ppm; δ_{H3} = 3.39 ppm), the methylene groups (4), (5), and (6) did not overlap between PEG in solution and in the hydrogel. A signal corresponding to free NHS ($\delta_{C6'}$=27.9 ppm; $\delta_{H6'}$=2.76 ppm) indicated the release of NHS from the PEG molecule. In addition, the methylene groups (4) and (5) exhibited a downfield shift in the carbon dimension in the hydrogel compared to PEG in solution resulting in a single signal at $\delta_{C4/5}$=34.1 ppm; $\delta_{H4/5}$=2.86 ppm. This indicates that these two methylene groups now share a similar chemical environment. This change in chemical shift is likely due to the formation of a crosslink between PEG and DGL, which introduces an NH group near methylene (5), thereby creating an almost symmetrical environment for groups (4) and (5). Moreover, a new signal at δ_{C7}=39.6 ppm; δ_{H7}=3.02 ppm likely represents the methylene group in the newly formed chain with DGL, which is closest to PEG and matches with predictions. Thus, solid-state NMR confirms the presence of the crosslink between DGL and PEG in the hydrogel and the release of NHS.

Table 2. Elastic modulus (E'), loss modulus (E''), and swelling ratio of DGL/PEG hydrogels of various concentration and ratio.

DGL/PEG (mM)	DGL:PEG ratio	Elastic modulus (kPa)	Loss modulus (kPa)	Swelling
1/25	1:25	12.0 ± 2.4	1.0 ± 0.3	20.8 ± 0.4
1.6/25	1:16	18.3 ± 2.2	2.5 ± 0.4	19.4 ± 2.3
2/19	1:10	30.6 ± 2.6	4.9 ± 0.8	19.7 ± 2.6
2/25	1:12	54.7 ± 3.1	8.6 ± 1.2	14.6 ± 0.7
2/37	1:16	105.5 ± 11.5	18.5 ± 3.4	11.1 ± 0.1
2/50	1:25	157.8 ± 14.1	40.9 ± 9.6	8.6 ± 0.4

The elastic (E') and loss (E'') moduli of 2D hydrogels with various compositions were determined at 1 Hz frequency with a 50 µm amplitude. The modulation of DGL/PEG ratio and concentration from 1/25 to 2/50 mM DGL/PEG allowed the stiffness modulation from 12.0 ± 2.4 kPa (1/25 mM DGL/PEG) to 157.8 ± 14.1 kPa (2/50 mM DGL/PEG; Figure 1(c) and Table 2). For all hydrogels compositions, E' was greater than E'' whatever the concentration and ratio used (Figure 1(d)) confirming the realization of self-standing hydrogels. Interestingly, while a proportional increase in PEG concentration for a given DGL concentration induced a linear elastic modulus increase (Figure 1(e), $R^2 = 0.9998$), a proportional increase in DGL concentration for a given PEG concentration triggered an exponential rise of E' (Figure 1(f), $R^2 = 0.8702$). These results suggest that the DGL has a predominant control over the hydrogel stiffness and appears to be the limiting molecule in the reaction.

The swelling properties of the hydrogels were determined in PBS at 37°C to mimic physiological conditions (Figure 1(g)). An increase in the DGL/PEG concentration and molar ratio triggered a decrease in hydrogels swelling, as reflected by the PBS absorption going from 2000% to 800% of the hydrogels dry weight for 1/25 and 2/50 mM DGL/PEG, respectively. In conclusion, the modulation of both DGL and PEG concentration and their ratio enables precise control of the stiffness and the water absorption of the resulting hydrogels (Table 2).

Effect of DGL/PEG hydrogel substrate stiffness and composition on the behavior of murine muscle cells

Taking advantage of the DGL/PEG hydrogel versatility, the proliferation and differentiation of murine myoblasts (C2C12 cells) was assessed on 2D flat hydrogels with different stiffness and molar ratios (Figure 2(a)). First, the ability of C2C12 myoblasts to proliferate on different hydrogels compositions was assessed by the evolution of cell confluency over time. We observed that under almost all the conditions, except for the softer 1/25 mM DGL/PEG hydrogel, C2C12 myoblasts normally expanded, and this ability was correlated with the hydrogel stiffness (Figure 2(b) and (c)). Indeed, the stiffer the hydrogel, the higher the cell confluency, peaking at 105.5 ± 11.5 kPa for the 2/37 mM DGL/PEG condition. However, in the 2/50 mM DGL/PEG condition, although being stiffer, myoblasts confluency was reduced, indicating a possible threshold value condition. In the 2/25 and 2/37 mM DGL/PEG conditions, C2C12 myoblasts covering 35 ± 9% and 43 ± 9% of the area respectively, were not statistically different from the plastic dish used as a positive control (in which cells covered 35 ± 8% of the area). As myoblasts spreading and elongation are sensitive to the substrate stiffness *in vitro*,[40] we next evaluated C2C12 myoblasts spreading, 30 h after cells seeding (Figure 2(d); S2). Myoblasts were well spread out and spindle-shaped, except for the 1/25 mM DGL/PEG condition which exhibited round-shaped cells associated with small spreading areas (Figure 2(d)).

We finally addressed if the mobility of C2C12 myoblasts on DGL/PEG hydrogels was affected compared to the control plastic substrate (Figure 2(e)). We first confirmed that hydrogels facilitate cell displacement, except for the softer condition (1/25 mM DGL/PEG; Figure 2(e)). Interestingly, while the stiffness drove C2C12 proliferation, their morphology and migration on the support were linked to hydrogel compositions, through the amount of DGL relative to PEG. On hydrogels with 1:25 and 1:10 DGL:PEG molar ratios, C2C12 myoblasts were less mobile and presented a smaller area compared to cells plated on hydrogels with 1:16 and 1:12 DGL:PEG molar ratios, which were similar to the positive plastic dish control (Figure 2(d) and (e)). This first approach allowed to discard the 1/25 mM DGL/PEG hydrogel condition as no cell proliferation or mobility was observed (Figure 2(d), (d), and (e)) and permitted to next assess myoblasts differentiation capacity.

C2C12 myoblasts were thus induced to differentiate into fusing cells by switching the media to low serum condition[41] (Figure 2(f)). Under these conditions, myoblasts exit the cell cycle and become myocytes, specialized cells with the potential to fuse with each other, forming multinucleated myotubes, which can be easily detected by their specific myosin expression.[42] Six days after serum depletion, myotubes were formed on almost all DGL/PEG hydrogels as shown by the myosin heavy chain staining (MyHC; Figure 2(f)). In 2/19 mM DGL/PEG condition,

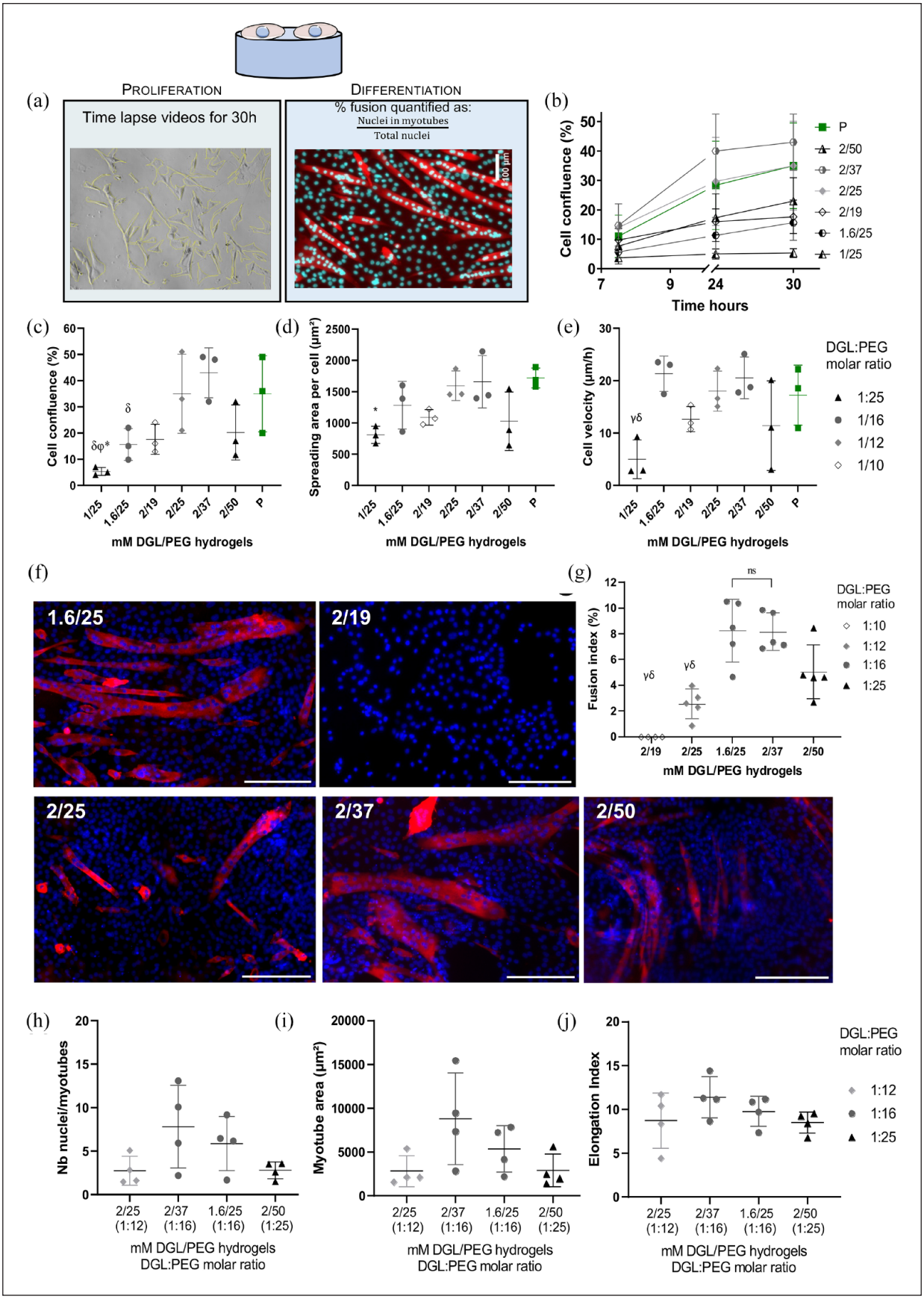
(a)
PROLIFERATION
DIFFERENTIATION
Time lapse videos for 30h
% fusion quantified as:
Nuclei in myotubes
Total nuclei
100 µm
(b)
Cell confluence (%)
Time hours
P
2/50
2/37
2/25
2/19
1.6/25
1/25
(c)
Cell confluence (%)
mM DGL/PEG hydrogels
(d)
Spreading area per cell (µm²)
mM DGL/PEG hydrogels
(e)
Cell velocity (µm/h)
mM DGL/PEG hydrogels
DGL:PEG molar ratio
1:25
1:16
1:12
1:10
(f)
1.6/25
2/19
2/25
2/37
2/50
(g)
Fusion index (%)
ns
mM DGL/PEG hydrogels
DGL:PEG molar ratio
1:10
1:12
1:16
1:25
(h)
Nb nuclei/myotubes
mM DGL/PEG hydrogels
DGL:PEG molar ratio
(i)
Myotube area (µm²)
mM DGL/PEG hydrogels
DGL:PEG molar ratio
(j)
Elongation Index
mM DGL/PEG hydrogels
DGL:PEG molar ratio
DGL:PEG
molar ratio
1:12
1:16
1:25

(Continued)

Figure 2. C2C12 myoblasts behavior on DGL/PEG hydrogels of various stiffness and compositions: (a) Myoblasts were cultured 30 h in proliferative condition and then switched culture for six more days in serum-depleted medium for six more days. (b) C2C12 myoblasts confluence over time on various DGL/PEG hydrogels in proliferative conditions. (c) Cell confluence and (d) cell spreading area and (e) cell velocity for 24 and 30 h post myoblasts seeding, as a function of DGL/PEG hydrogel concentration and ratio (mM DGL/PEG). F) Representative images of C2C12 myotubes on 2D flat DGL/PEG hydrogels stained for Myosin Heavy Chain (Red, MyHC) and Dapi (Blue, cell nuclei). Scale bar = 200 m. (g) Fusion index as a function of hydrogel concentration (mM DGL/PEG), after 6 days in serum depleted medium. (h–j) C2C12 myotubes quantifications after 6 days in serum depleted medium as a function of hydrogel concentration (mM DGL/PEG): (h) nuclei per myotubes, (i) myotubes area quantification (j), and elongation index (Feret's diameter/width; left). P: Plastic dish. C, D, E, G: One-way ANOVA + Tukey's multiple comparison $p < 0.05$ compared to γ: 1.6/25; Φ: 2/25, δ: 2/37, * Plastic dish.

which has the highest proportion of DGL relative to PEG (i.e. 1:10, Table 2), no myotubes were formed after 6 days although it exhibited a 80% cell confluency, compatible with cell fusion conditions. We first quantified myoblasts fusion capacity on hydrogels (fusion index), by evaluating the percentage of nuclei present in myotubes (cells with a positive staining for myosin heavy chain (Figure 2(g)). We found that hydrogels with the same DGL: PEG ratio (i.e. 1.6/25 and 2/37 mM DGL/PEG) display the highest fusion capacity. This myogenic capacity of these two hydrogels composition was confirmed using other parameters such as the average number of nuclei inside myotubes (Figure 2(h)), the mean area of myotubes (Figure 2(i)), and the myotube elongation (Figure 2(j)). Thus, the fusion capacity of C2C12 myoblasts on hydrogels appeared to be related to the DGL:PEG ratio and unrelated to substrate stiffness as hydrogels with different elastic moduli but with the same DGL: PEG ratio (i.e. 1.6/25 and 2/37 mM DGL/PEG at 18.3 ± 2.2 and 105.5 ± 11.5 kPa, respectively) showed a similar fusion index of $8.2 \pm 1.1\%$ and $8.1 \pm 0.7\%$, respectively. What is more, conditions with a smaller fusion index, and thus, smaller amount of PEG with DGL:PEG molar ratio of 1:10 and 1:12 exhibited myotubes with a decreased nuclei content by myotubes, smaller myotube areas with a limited elongation (Figure 2(h–j)).

The increasing amount of DGL inside DGL/PEG hydrogels was thus related to a decrease in cell ability to spread out and to fuse on substrates, suggesting that the DGL could have an influence on cell behavior. To confirm the above-mentioned assumptions, C2C12 myoblasts were studied on saturated DGL-coated surfaces on which the resultant stiffness is provided by the polystyrene beneath and is not varied. Myoblasts grown on DGL coatings or on plastic dish showed no significant variation in metabolic activity after 120 h in proliferation (Supplemental Figure S3A). Cells grown on Matrigel showed increased metabolic activities, linked to the presence of proteins, growth factors, and protease in the Matrigel composition, which collectively contribute to its biological activity.[43] A similar fusion index was observed for myoblasts cultured on Matrigel or on crude plastic dish, with $23.3 \pm 1.5\%$ and $26.5 \pm 2.3\%$, respectively. However, it dropped to $4.1 \pm 0.9\%$ on DGL-coated polystyrene as reflected by an 85% decrease of the fusion index compared to cells on plastic dish (Supplemental Figure S3B). In addition to the fusion impairment, DGL coatings affected myotubes morphology and fusion, which exhibited a smaller area with fewer nuclei compared to myotubes on the uncoated plastic dish control (Supplemental Figure S3C and D). These results confirm the predominant role of the DGL within the DGL/PEG hydrogel on C2C12 myoblasts fusion capacity.

Evaluation of the 3D induced DGL/PEG hydrogel structure for myoblasts growth and differentiation

The desired function of any implanted material, particularly in VML, is to allow muscle and vessel cells infiltration that will prevent necrosis, support tissue formation and functional outcome.[13] Based on our results (Figure 2), only the three conditions associated with an increased proportion of PEG compared to DGL (i.e. 1.6/25, 2/25, and 2/37 mM DGL/PEG conditions) were selected for further myogenesis-related analysis into 3D hydrogels conditions. Due to the tight mesh size of the DGL/PEG hydrogel (<10 nm[44]), an adapted porosity is required to enable cells penetration and replicate the intricate native 3D signals provided by the physiological extracellular matrix. The three selected conditions of DGL/PEG hydrogel were thus rendered porous to form a 3D structure through an effervescent approach as described previously.[22] Effervescent porous hydrogels (EPH) could be easily formulated through a straightforward single-step injection using dual-chamber syringe. After crosslinking, hydrogels of 75%–80% porosity can be obtained, with an average pore size of about 300 µm and extensive pore interconnection, with windows of interconnection reaching 130 µm. We therefore assessed the ability of the porous structures to support skeletal muscle cell infiltration using C2C12 myoblasts seeded at a density of 20,000 cell/cm² on the top of EPH (Figure 3(a)). After 7 days in proliferative conditions, cells populated the entire 2 mm-thick structure, confirming the suitability of the 3D interconnected structure to allow rapid cell entry and colonization (Figure 3(b)). Proliferative C2C12 myoblasts were therefore allowed to colonize the entire scaffold before cell differentiation was induced by immersing

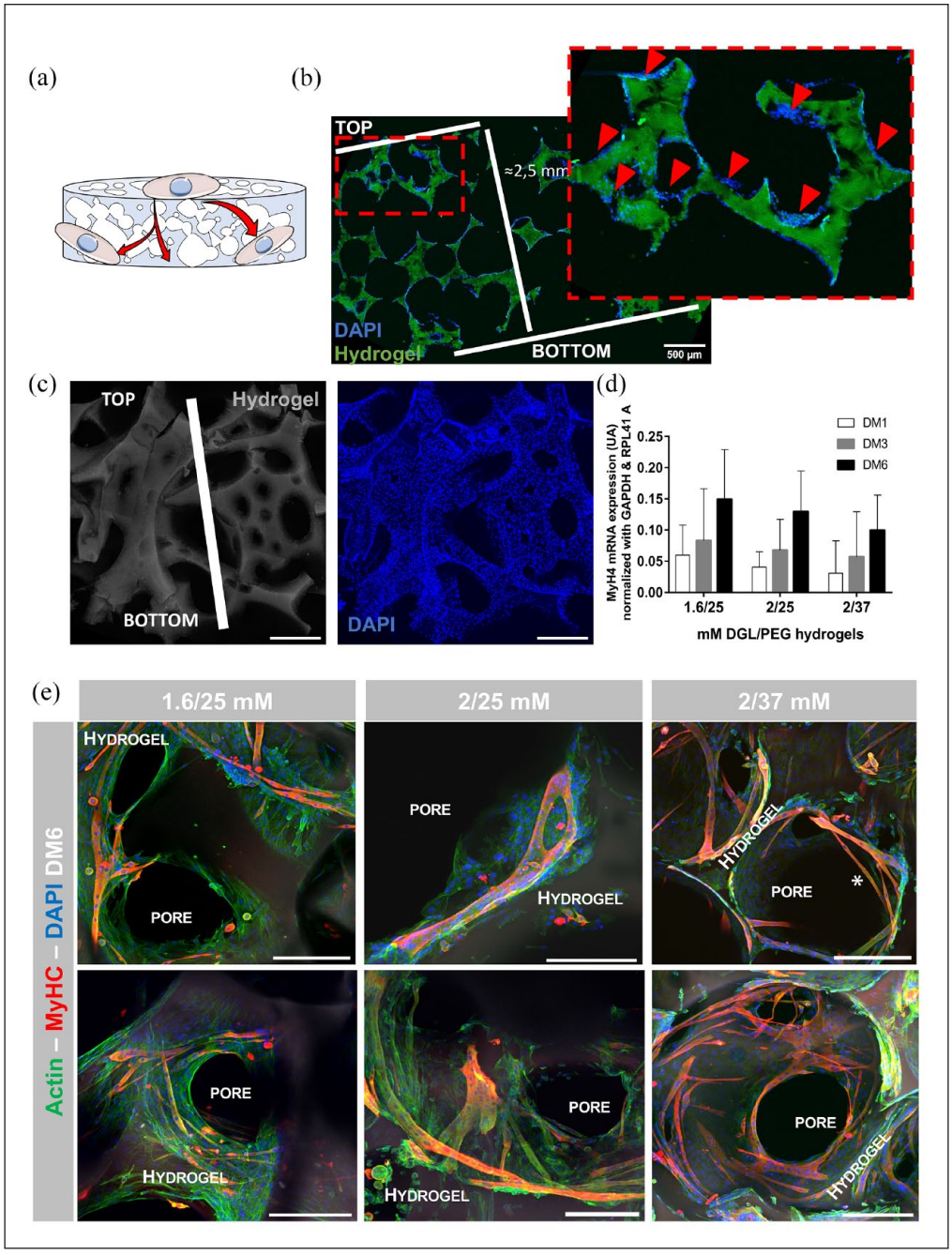

Figure 3. C2C12 myoblasts behavior inside EPH of various concentrations: (a) scheme of the procedure for the cell culture. (b) Representative images of C2C12 myoblasts repartition inside a 2/25 mM DGL/PEG EPH after 7 days in proliferative conditions (myoblasts nuclei in blue and hydrogel in green) and close up (red dashed rectangle) with red arrows pointing at cell nuclei accumulation. (c) Representative images of C2C12 repartition inside a 2/25 mM DGL/PEG EPH after 7 days in proliferative conditions and 6 days in serum-depleted medium (cell nuclei in blue and hydrogel in grey). Scale bar = 400 m. (d) Quantification of MyH4 mRNA expression after 1, 3, and 6 days after serum depletion on various EPH conditions. One-way ANOVA + Tukey's multiple comparison. (e) Representative images of myotubes inside EPH of various DGL/PEG compositions stained for actin cytoskeleton in green, myosin heavy chain (MyHC) in red, cell nuclei in blue, and hydrogel in dark gray). Scale bar = 200 m.

the 3D scaffolds in serum-depleted medium. After an additional 6 days in these differentiation conditions, myoblasts nuclei were still observed throughout the entire depth of the hydrogels, validating a homogeneous distribution within the EPH (Figure 3(c)). The commitment of myoblasts into the differentiation process was evaluated by the quantification of the expression of a specific myogenic gene (Myosin heavy chain 4, MyH4)

Table 3. Quantification of C2C12 fusion index (% of nuclei in MHC positives myotubes), myotube area and elongation index (Feret diameter/width) after 6 days in serum depleted medium inside 3D EPH of various concentration and molar ratio (mM DGL/PEG).

DGL/PEG (mM)	DGL: PEG ratio	Fusion index	Area (μm²)	Elongation index
1.6/25	1:16	8.3 ± 3.3	3694 ± 1231	13.7 ± 3.3
2/25	1:12	9.8 ± 0.7	5221 ± 416	15.6 ± 1.8
2/37	1:16	9.1 ± 2.6	4276 ± 1044	16.8 ± 1.4

One-way ANOVA + Tukey's multiple comparison show no statistical differences among data.

using RT-qPCR after 1, 3, and 6 days in differentiation conditions. As expected, our results indicated a time-dependent increase of MyH4 expression, consistent across all studied EPH conditions, confirming that the selected EPH are a favorable substrate for muscle cells differentiation (Figure 3(d)).

We next questioned myotubes morphology and their localization inside the EPH using confocal microscopy approach. The images confirmed the ability of C2C12 myoblasts to fuse and form multinucleated myotubes, as revealed by the myosin heavy chain staining, in all EPH conditions (Figure 3(e)). Notably, for the three conditions, myotubes were present throughout the entire 2 mm thick EPH, further confirming the C2C12 myoblasts fusion capacity throughout and in the depth of the EPH. To better appreciate the characteristics of the formed myotubes, different parameters such as the fusion index, myotubes mean area, and myotubes elongation were quantified (Table 3). The 2/25 mM DGL/PEG EPH condition exhibited the best ability to sustain C2C12 myoblasts fusion in 3D, despite showing comparatively lower fusion support in 2D. Consequently, within the EPH, lower DGL: PEG (1:16) molar ratios were less likely to promote cell fusion and form large myotubes compared to the higher DGL: PEG (1:12) molar ratio (Table 3). For the softer condition (i.e. 1.6/25 mM DGL/PEG), myotubes area was smaller than for stiffer conditions (i.e. 2/25 and 2/37) although not significantly (Table 3). Overall, myotubes area quantification indicated larger myotubes into 2/25 mM DGL/PEG EPH.

For all EPH conditions studied, myotubes shape adapted perfectly to the curvature of the pores obtained (visible on Figure 3(e), 2/37 mM DGL/PEG condition, bottom) suggesting that a rounded, curved structure also supports myotubes elongation. Interestingly, some myotubes were observed with no continuous contact with the substrate (visible on Figure 3(e), 2/37 mM DGL/PEG condition, top, asterisk), suggesting that curvature promotes myotube detachment and/or strong anchoring of the tip of myotubes to the support, reflecting potentially better myotubes maturation (Figure 3(e)). In summary, EPH guided the growth and differentiation of C2C12 myoblasts cells, indicating a suitable environment for both myoblasts proliferation and myotubes differentiation.

Validation of the myogenic potential of EPH using primary human myoblasts

To confirm the broad myogenic capacity of the designed EPH, the behavior of primary human myoblasts (pHMs) was investigated to provide a further step toward the characterization of EPH potential. Based on our results, we set aside the 1.6/25 mM DGL/PEG EPH condition for further studies as it showed the lowest fusion and elongation capacity.

Purified pHMs were seeded onto 2/25 and 2/37 EPH and their ability to form multinucleated myotubes inside EPH was appreciated using confocal microscopy analysis (Figure 4). pHMs demonstrated a similar aptitude to infiltrate the 2 mm thick, porous structures as observed with murine C2C12 myoblasts, confirming the EPH suitability for infiltration, colonization, and proliferation of cells from different origins, including human cells. After a proliferation phase, pHMs culture media was switched to a serum-depleted medium for either 6 or 10 days (respectively DM6 and DM10). In these conditions, the majority of pHMs had fused into myotubes within the different EPH, as indicated by the staining of both myosin heavy chain (MHC) and desmin in cells with multiple nuclei, confirming the pro-fusiogenic potential of the two selected EPH conditions (Figure 4(a)). Moreover, the EPH were able to support the fusion of pHMs in a well longitudinal organized manner. Some multinucleated cells exhibited intrinsic alignment within individual pores (exemplified in Figure 4(a), 2/25 mM DGL/PEG condition).

In addition, akin to C2C12 cells, some myotubes were lifted off from the substrate, bridging pore edges, as shown in Figure 4(a) under the 2/37 mM DGL/PEG condition. These "crossing myotubes" are potentially induced by their detachment from the support as maturation progresses and could thus indicate a better achievement of the myofibrillogenesis, giving the possibility for these "mature" myotubes (i.e. myofibers) to spontaneously contract. To explore this possibility, myotubes were allowed to mature for 10 days in the EPH and were monitored using conventional microscopy. As shown in Supplemental Videos 1 and 2, deformation of the EPH was observed upon myofibers contraction, starting after 6 days of differentiation. These results indicate that the EPH not only supports myofiber contraction but also adjusts to the tension

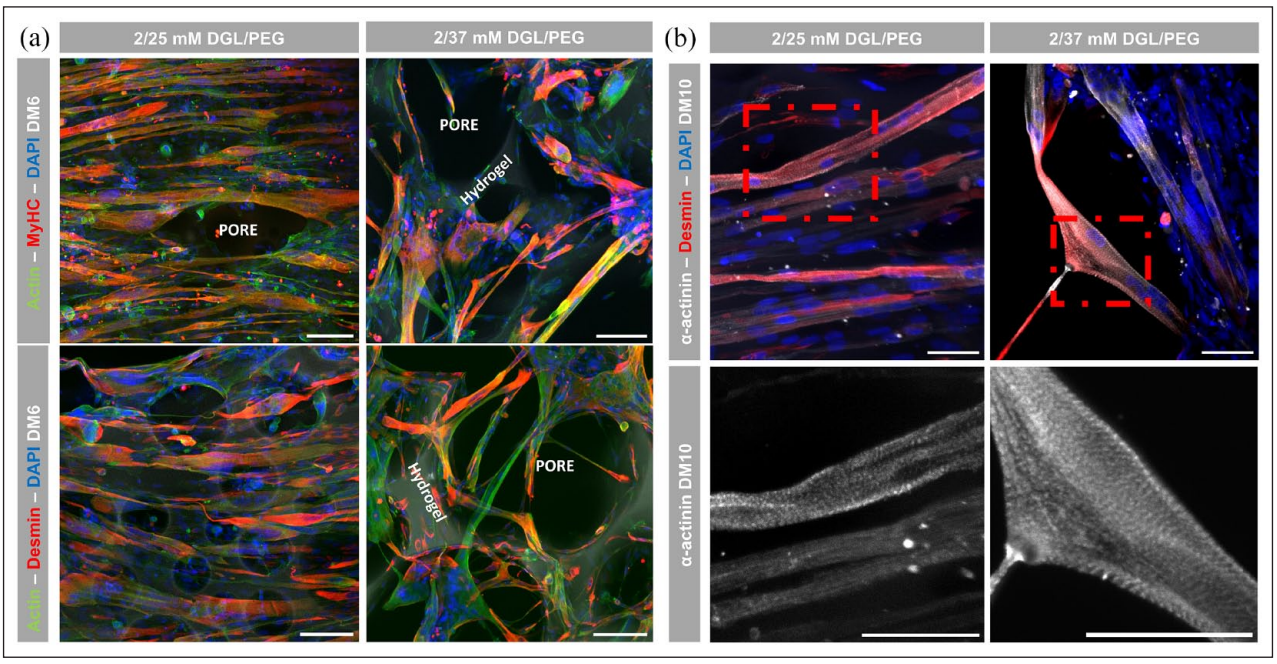

Figure 4. Primary humans muscle stem cells (pHMs) behavior inside EPH of various DGL/PEG concentrations: (a) pHMs plated onto 2/25 or 2/37 mM DGL/PEG EPH after 6 days in serum depleted medium (DM6). Cells were stained for either Myosin Heavy Chain (red, MyHC, top) or desmin (red, bottom), actin in green and dapi, in Blue (cell nuclei). Scale bar = 100 m. (b) pHMs plated onto 2/25 or 2/37 mM DGL/PEG EPH after 10 days in serum depleted medium (DM10). Top: images of cells stained for desmin (red), α-actinin in gray and dapi, in blue (cell nuclei). Bottom: close up of red dashed rectangle (top) pointing α-actinin striation. Scale bar = 50 m.

exerted by myofibers on the environment. This reached step of myotubes maturation into myofibers was confirmed using confocal microscopy, which showed striated staining for α-actinin protein within desmin positive multinucleated cells (Figure 4(b)).

Taken together, the maturation of myotubes into myofibers with contractile capacity within the EPH supports their potential to sustain muscle formation and, consequently, the regeneration process *in vivo*.

In vivo evaluation of the EPH in the repair of large rat muscle defects

Based on our experiments realized with murine and human myoblasts on 2D and 3D conditions (Figures 2–4), we selected the 2/37 mM DGL/PEG EPH condition to assess its suitability when directly injected into large muscle defects and its subsequent interaction with the muscle regeneration process. Defects of 5 mm were created in the Tibialis anterior muscle of Wistar rats (Figure 5(a)). EPH were injected through a 21 G needle into the created muscle defect (Supplemental Video 3). Ten seconds post-injection, hydrogel crosslinking provided porosity formation and structural rigidity before wound suturing. Twenty-four hours after surgery, the animals were able to walk, with no signs of sepsis, infection, or visible pain. Upon excision of the injected implants after 7 or 21 days, EPH appeared well integrated into the defect site, with no fibrous capsule formation (Figure 5(b)). Granulation tissue was evident directly around the injected porous hydrogels, extending to the edges of the seemingly original defect (Figure 5(b), arrows). The in situ-created porosity within the injected EPH was visible, accompanied by a clear cellularization inside the porous structure (Figure 5(b), WGA staining). After 21 days, the granulation tissue was significantly reduced, muscle fibers reached hydrogel edges, and extensive cellularization occurred within the scaffold's pores. In non-injected muscles defects (empty defects), similar granulation tissue was observed at 7 days. By 21 days, however, the granulation tissue was almost resolved, making it challenging to pinpoint the original defect location by histology.

EPH injection into the muscle defect allowed in-situ porous structure formation exhibiting polydisperse sizes and a mean ranging between 123 and 151 µm (Figure 5(c)), with a quantifiable pore density close to 50 per mm2 (Figure 5(d)). The number of pores did not significantly decrease over implantation, indicating that the porous structure remains stable, at least for 21 days. This was confirmed by a similar surface of injected EPH in serial cross-sections of the muscle defects after 7 and 21 days (Figure S4). Highlighting pore interconnection, extensive cellular

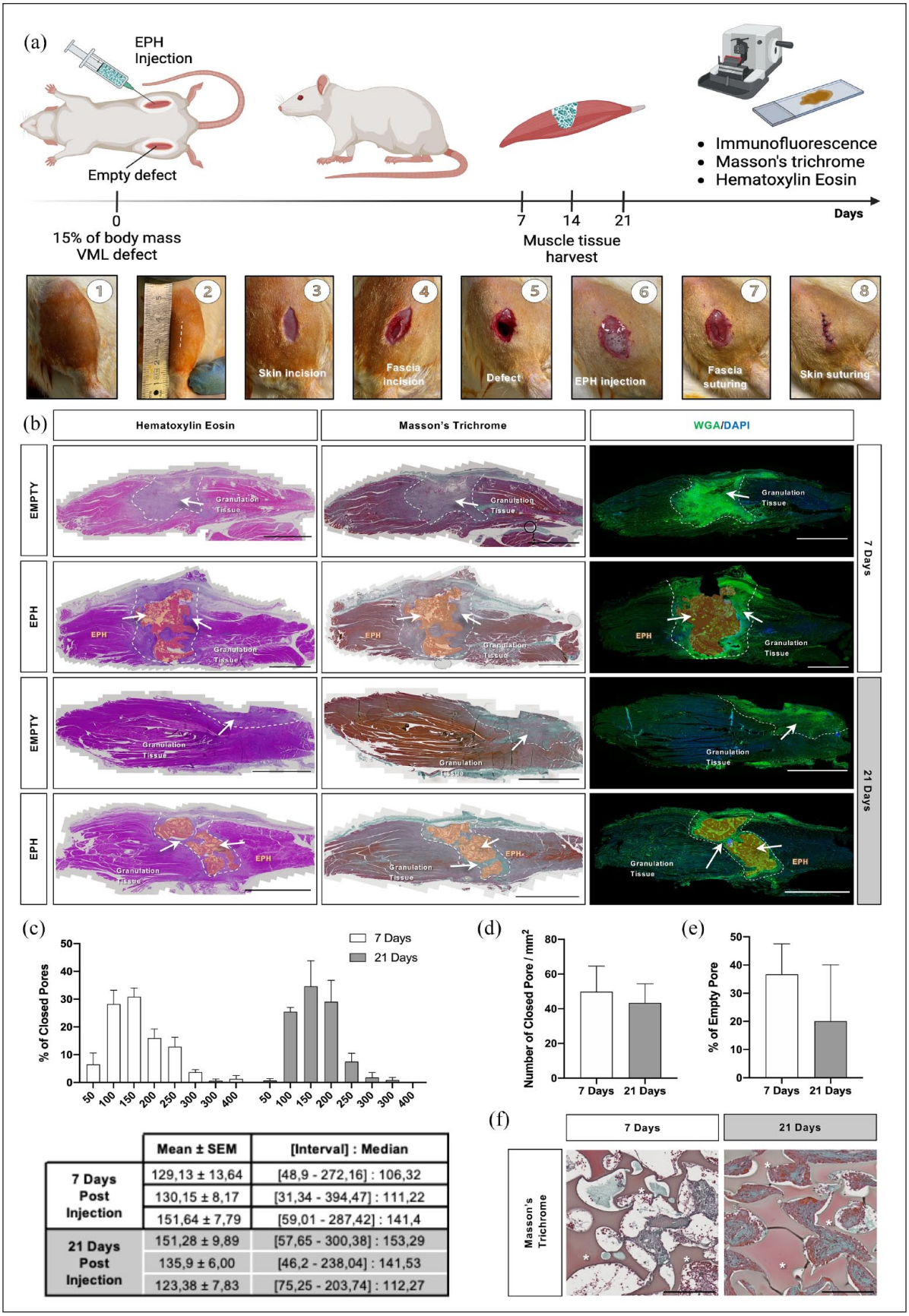

	Mean ± SEM	[Interval] : Median
7 Days Post Injection	129,13 ± 13,64	[48,9 - 272,16] : 106,32
	130,15 ± 8,17	[31,34 - 394,47] : 111,22
	151,64 ± 7,79	[59,01 - 287,42] : 141,4
21 Days Post Injection	151,28 ± 9,89	[57,65 - 300,38] : 153,29
	135,9 ± 6,00	[46,2 - 238,04] : 141,53
	123,38 ± 7,83	[75,25 - 203,74] : 112,27

(Continued)

Figure 5. EPH suitability and fate in a muscle defect: (a) Scheme of the experimental design, images of rat tibialis anterior muscle defect and EPH injection procedure. (b) Hematoxylin Eosin (HE), Masson's Trichrome (TM) and Wheat-Germ Agglutinin (WGA) staining of whole TA muscle harvest at two distinct time points (7- and 21-day post-implantation). Images provides a macroscopic view of tissue morphology and the spatial distribution of the injected EPH constructs within the muscle tissue (highlighted in orange). Injured-healthy muscle interfaces are indicated by dashed lines. All scale bars = 500 μm. (c; up) Closed pore size distribution, in μm, of EPH in muscles ($n = 3$); (bottom) Closed pore mean diameters characteristics after 7 and 21 days, in μm ($n = 3$). (d) Closed circular pore density within EPH over implantation time, refers to the density of circular-shaped pores within the EPH implants. (e) Percentage of empty pores within EPH at 7- and 21-day post-implantation, giving information on the rate of cellular infiltration and scaffold degradation. (f) Representative Masson's trichrome staining showing cellularized pores within the EPH over implantation. EPH is annotated with an asterisk (*).

infiltration reached 65% of quantified pores after 7 days and 80% after 21 days (Figure 5(e)). In addition to cellularization, tissue formation was visible within the pores, featuring significant collagen deposits (Figure 5(f), in green). Fibroblast-like cells with elongated phenotype were also observed within the hydrogel, in close contact with collagen sites.

Immunofluorescence and immunohistochemical analyses were realized to better characterize the various cell populations inside the EPH pores, or at the interface between the granulation and the muscle tissues (Figure 6). In the granulation tissue, a high density of inflammatory cells was present (granulocytes or lymphocytes) and macrophages. Within the EPH pores, these inflammatory cells were concentrated at the proximity of the hydrogel, with evidence of phagocytosis. A staining for M1 (CD11) and M2 macrophages (CD206) revealed the presence of both cell's types, with a predominance of M2 type and cells expressing both markers (Figure 6(a)). Extensive vascularization was observed within the pores and throughout injected EPH, confirmed by specific staining for type IV collagen (Figure 6(b)). We next investigated the presence of muscle cells and myotubes inside the EPH (Figure 6(c) and (d)). Supporting our *in vitro*-based observations of hydrogel ability to sustain myoblast adhesion and proliferation, we observed *in vivo*, MyoD+ mononucleated myoblasts dispersed within the porous hydrogel (Figure 6(c) and (d)). However, their distribution varied significantly from one pore to another. Moreover, we identified two distinct multinucleated muscle cell populations within the EPH: (1) multinucleated cells, negatives for MyoD staining, with an amount of myonuclei between 10 and 20 that remain aggregated in the center of myotubes (Figure 6(c), cropped areas no. 1–5, orange arrows). In alignment with the heterogeneous distribution of mononucleated MyoD+ myoblasts within the hydrogel, these myotubes are also unevenly dispersed. However, these myotubes were located at a significant distance from the injury site (Figure 6(c), cropped area no. 1), confirming the EPH's ability to support MuSC cells entry, proliferation, and subsequent muscle cell formation and fusion (Figure 6(e), dash circle). (2) Multinucleated cells, positives for MyoD staining, with either centralized or peripheral myonuclei positioning, reflecting ongoing fusion of muscle cells at different level of formation/maturation (Figure 6(c), cropped areas no. 2–5, white arrows). These myotubes/myofibers are mainly found within the peripheral pores of the hydrogel or at the transition zone between porous hydrogel and remaining muscle tissue. It suggests that the hydrogel also favors skeletal muscle fibers anchoring and regeneration at its periphery. Indeed, in comparison to the surrounding muscle tissue, the staining suggests a more pronounced alignment of the muscle fibers near the EPH (Figures 5(b) and 6(c)). To quantify this observation, we assessed the orientation of the muscle tissue at the vicinity of the injury site, with or without the EPH (Figure 6(f)). The proportion of surrounding muscle tissue with aligned myofibers compared to non-aligned myofibers was less than 50%, 7 days after injury without EPH and this ratio decreased to 30%, 21 days post-injury. However, the presence of EPH correlates with improved organization at both 7- and 21-day post-injury, with more than 75% of the surrounding tissue containing aligned muscle fibers (Figure 6(f)). This result suggests that, without EPH, the presence of granulation tissue near the regenerated muscle tissue areas favor the local disorganization of muscle fibers, disrupting their continuity and organization, and thus, contributing to the muscle dysfunction. Therefore, the selected EPH composition, when present at the injury site, (i) promotes the anchoring of the remaining preserved muscle tissue to the EPH or (ii) aid in the transition from the muscle necrosis stage to the regeneration stage, thus maintaining an organized muscle tissue near the site of lesion.

Discussion and conclusion

Although the scientific community has extensively investigated various approaches to improve muscle healing, there is still no gold standard treatment.[45] This study aims to evaluate a synthetic acellular biomaterial as a support to enhance skeletal muscle regeneration. To this aim, we have tested *in vitro* various compositions and ratios of a synthetic DGL/PEG-based biomaterial. Our objective was to adapt the biomaterial to support the attachment, proliferation, and differentiation of muscle cells. After selecting the most suitable composition, we investigated its application *in vivo* into large muscle defects. Here, we discuss the

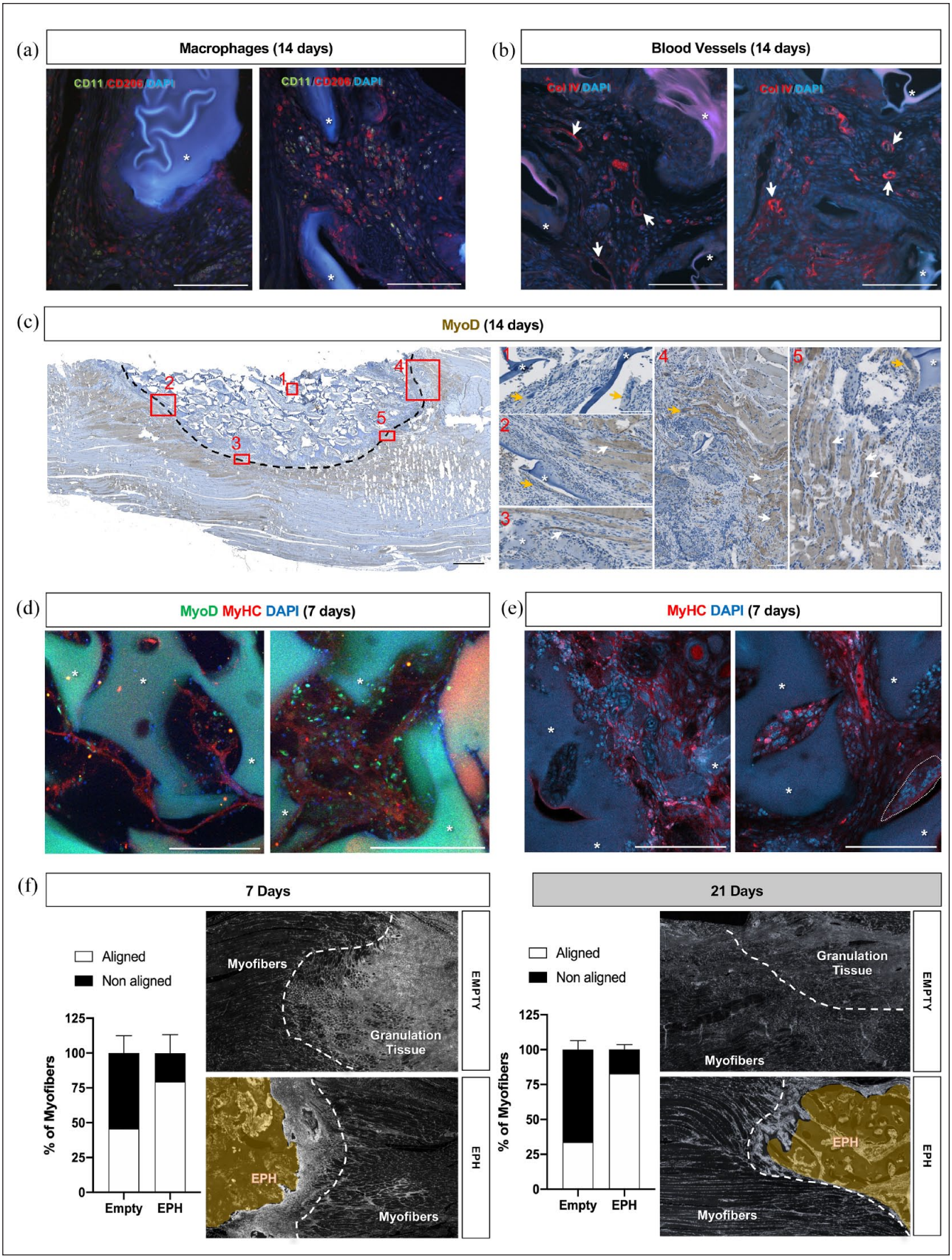
(a)
Macrophages (14 days)
CD11/CD206/DAPI
CD11/CD206/DAPI
(b)
Blood Vessels (14 days)
Col IV/DAPI
Col IV/DAPI
(c)
MyoD (14 days)
1
2
3
4
5
(d)
MyoD MyHC DAPI (7 days)
(e)
MyHC DAPI (7 days)
(f)
7 Days
21 Days
Aligned
Non aligned
% of Myofibers
125
100
75
50
25
0
Empty
EPH
Myofibers
Granulation Tissue
EMPTY
EPH

(Continued)

Figure 6. Microenvironmental characterization and cellular dynamics toward the EPH implants: (a) Representative images of immunofluorescence staining for M1 (CD11) and M2 (CD206) macrophages, and (b) blood vessels (collagen type IV). Scale bar = 200 m. (c) Right: representative images depicting MyoD immunohistochemistry. Scale bar = 500 m. Left: cropped area from the right panel, white arrows point multinucleated cells, positives for MyoD with centralized/aligned myonuclei; orange arrows point multinucleated cells, negatives for MyoD with aggregated myonuclei. EPH is denoted with an asterisk (*). Scale bar = 100 m. (d and e) Representative images illustrating immunofluorescence staining of muscle cells (MyoD in green and MyHC in red). EPH is denoted with an asterisk (*) and dapi: in blue. Multinucleated cell with aggregated myonuclei is circled with dash lines. Scale bars = 200 μm. (f) Percentage of aligned and non-aligned myofibers at 7- and 21-day post-muscle defect with EPH injection compared to empty defects. Injured-healthy muscle interfaces are indicated by dashed lines.

implications of our findings and their relevance for myogenesis and skeletal muscle regeneration.

It is well known that myoblasts cells sense substrate stiffness and, depending on the rigidity of the support, myotubes differentiation and myofibrils formation will be influenced.[40] One of the main challenges in skeletal muscle regeneration, is designing muscle-tissue-optimized supports with stiffness adapted to the complex behavior of muscle cells. This is especially crucial as many cell types, when grown on soft matrices, exhibit minimal adhesion, resulting in less spreading, reduced proliferation rates and a minimal actin stress fibers formation. Conversely, rigid matrices induce increased cells spreading with focal adhesions and formation of actin stress fibers, negatively impacting their mobility.[46] Similarly, too soft or too rigid matrices impair myofibrils formation.[40] Our DGL/PEG hydrogel composition can be tailored to exhibit a range of rigidities from 12 to 160 kPa and a range of DGL:PEG ratio from 1:25 to 1:10, both influencing myoblasts morphology, proliferation, and mobility (Figures 1 and 2). These results are in accordance with previous observations on fibroblasts where the amount of DGL in the DGL/PEG hydrogel played a critical role on cells adhesion, morphology, and viability.[26] DGL's influence on cells is related to cationic charges brought by NH2 groups present on DGL surface.[47] Cells use adhesion sites to contract the cell body forward[48] and be able to migrate on supports. This increase in cells adhesion could thus lead to the myoblasts decreased propensity to migrate on DGL/PEG hydrogels of high DGL concentrations.

In addition, myoblasts seeded on neutral surfaces display higher expression of myogenic factors in comparison with positively (NH2) and negatively (COOH) charged surfaces suggesting a better differentiation on neutral surfaces.[49] This decrease in the differentiation properties was related to an enhanced interaction of cells with NH2 moieties through $\alpha5\beta1$ and $\alpha v\beta3$ integrins.[49] In summary, this result confirms that an increased ratio of DGL in the DGL/PEG hydrogel led to higher levels of cationic charges, influencing both myoblast proliferation and subsequent differentiation (Figure S3). Increasing the amount of PEG-NHS, which reacts with NH2+ moieties, decreases the positive charges and restores C2C12 myoblasts fusion properties. Therefore, it is necessary to find an equilibrium in the DGL:PEG ratio to enable cell adhesion *via* cationic charges without being too elevated and inhibiting subsequent fusion process. These conditions have been found with conditions 1.6/25, 2/25, and 2/37 mM DGL/PEG hydrogels.

Overall, PEG-based hydrogels have gained considerable attraction in tissue engineering research over the recent years.[50] These hydrogels have demonstrated promise in mimicking the stiffness and mechanical characteristics of the muscle extracellular matrix, potentially facilitating the regeneration of myogenic tissue.[51] Our hydrogel stands out for skeletal muscle applications due to its unique formulation containing poly lysine dendrimers (DGL).[26] While synthetic biomaterials, such as PEG-based hydrogels, generally requires coating or mixing with natural materials such as fibrin, laminin, or Matrigel to promote cell attachment,[50] we offer a simplified and streamlined approach to scaffold design for skeletal muscle tissue engineering by integrating DGL directly into the hydrogel formulation. This eliminates the complexities associated with coating processes while enhancing its biocompatibility.

In addition to mechanical and biochemical cues, the biomaterial can bring topographical cues that enhance muscle regeneration through engineered 3D macroporosity. The curvature of the EPH provides suitable cues to enhance cell alignment upon fusion, suggesting that cells can perceive pores morphologies. To the best of our knowledge, this phenomenon has not been reported in the literature for non-aligned porosity such as our effervescently generated porous structure.[52,53] This is an interesting feature as a long-range organization of myoblasts is required to create a muscle architecture globally aligned to provide optimal muscle tissue functions. This phenomenon has already been described when myotubes are cultured on pillars, in which myotubes alignment exerted a passive tension, causing myotubes bundles to lift from the substrate.[54] In some instances, this passive tension also led to pillars being drawn closer together.[55] It was suggested that in the pillars system, attachment points mimicked tendons anchoring site within the musculoskeletal system. In the 3D DGL/PEG hydrogels, we observed the presence of "crossing myotubes" *in vitro*, which potentially arise after detachment from the support, as maturation progresses. We correlated this phenomenon with improved myofibrillogenesis (Figures 3 and 4). Our findings may be attributed to the stiffness of 2/25 and 2/37 mM DGL/PEG EPH

(35 ± 5.0 and 57.8 ± 3.5 kPa in compression respectively[22]), which is higher than the reported muscle tissue stiffness but close to the tendon ECM (shear modulus between 25 and 45 kPa[56]). Therefore, the EPH stiffness could mimic some tendon properties, providing specific signals to myotubes to thus exert passive tension on the support and enabling them to be lifted inside the porous structure.

Highlighting its ease of application, the EPH can be accurately injected into a created muscle defect, as demonstrated in Supplemental Video 3. Consistent with the effervescent-based system's characteristics,[22] a significant volume expansion occurrs during injection, effectively filling the defect. The effervescent-based volume expansion ensures an intimate contact between the continuous porous structure and the defect edges, accommodating a wide variety of complex shapes unlike other injectable hydrogels such as cryogels,[57] granular hydrogels,[23] or anisotropic hydrogels.[58] Ten seconds post-injection, hydrogel crosslinking provided porosity formation and structural rigidity before wound suturing. The presence of MyoD-positive cells within the EPH, a key regulator of myogenesis,[59] indicated the colonization of pro-fusiogenic cells and the initiation of muscle cells differentiation. Interestingly, these mononucleated cells, prone to fuse.[60,61] are essentially present within the EPH pores, 7 or even 14 days post-injury (Figure 6(a) and (d)) and lead to the formation of multinucleated cells, positives for MyHC, the motor protein of thick filaments[42] (Figure 6(d) and (e)). However, only myotubes with a limited number of myonuclei (between 10 and 20), were observed in depth of the EPH (Figure 6(c), cropped areas no. 1–5, orange arrows and Figure 6(e), dashed highlight). Since MyoD expression is downregulated in mature muscle fibers,[62,63] these multinucleated cells lacking MyoD staining can be considered as myotubes that have ended the fusion phase. These myotubes indicate that myoblasts were (a) able to colonize the EPH and (b) divide and fuse to form these myotubes within the EPH. Despite these observations, myotube fusion capacity appeared restricted regarding myonuclei number and their uneven distribution hindered significant muscle regeneration in the defect. To address this challenge, incorporating drug delivery strategies could offer a promising avenue to improve cell proliferation and thus enhance tissue regeneration.[64] One approach involves the incorporation of growth factors or cytokines known to promote muscle cell proliferation and differentiation. For instance, factors such as insulin-like growth factor (IGF), fibroblast growth factor (FGF), and transforming growth factor-beta (TGF-β) have demonstrated efficacy in stimulating myogenic precursor cell proliferation and differentiation.[65] By encapsulating these molecules within the EPH scaffold, we should provide sustained and localized delivery, optimizing their bioavailability and enhancing their biological effects on infiltrating cells. Furthermore, small molecule compounds targeting specific signaling pathways involved in muscle regeneration could be integrated into the EPH scaffold. For instance, compounds activating the Wnt/β-catenin pathway have been shown to promote myogenic differentiation and muscle regeneration.[66]

Another approach to enhance muscle cell colonization is through the gradual degradation of the scaffold after implantation. Studies have shown that controlled degradation is crucial to avoid inhibiting new tissue formation.[58,67] In our studies, when subcutaneously injected into mice, the DGL/PEG hydrogel was actively degraded by macrophages located at the periphery.[26] The degradation correlated with hydrogel stiffness: hydrogels of higher densities were less degraded than those of lower densities and stiffness, allowing partial control over the degradation rate. These findings were confirmed with effervescent porous hydrogels, which, upon direct sub-cutaneous injection, also experienced macrophages-driven degradation.[22] In this study, although the EPH hydrogels injected in the muscle defect were colonized by macrophages with evidence of phagocytosis, their observed degradation was limited by their selected composition and the short implantation period. However, based on our results and studies demonstrating that DGL can as well be degraded by endogenous peptidases,[68] the DGL/PEG hydrogel is intended to acts as a temporary scaffold that supports cell ECM production and gradually degrades to make way for newly formed tissue.

Overall, extensive cellularization, vascularization and tissue deposition observed within injected porous hydrogels align with previously published biocompatibility studies,[22] further confirming the suitability of the injectable structures to integrate into the natural healing processes. The important presence of pro-regenerative (M2) type macrophages suggests that porous hydrogels do not induce an exacerbated and sustained inflammatory reaction, which is the hallmark of pathological fibrosis and impaired muscle regeneration.[69,70] Instead, their presence allows the resolution phase of inflammation and muscle repair to proceed. Previously, immune responses to biomaterials were related to rejection[71]; however, subsets of innate immune cells have been identified as important mediators of scaffold remodeling and can be targeted for immune-mediated tissue regeneration.[72] The contribution of the EPH in the inflammatory response buffering to promote muscle regeneration needs to be further investigated.

As expected for acellular strategies,[15,23,73,74] the presence of myofibers inside the pores highlights the capacity of the EPH to sustain myoblasts adhesion, proliferation, and thus colonization within EPH pores. Surprisingly, we observed, outside of the EPH and close to the hydrogel interface, the presence of muscle fibers which do not exhibit centrally localized myonuclei and express heterogeneously MyoD regenerating marker (Figure 6(c)). Such myofibers, positives for MyoD, are alike regenerating or

newly formed myofibers, close to the interface between the EPH and the remaining muscle tissue. These myofibers suggests that the hydrogel itself favors either skeletal muscle fibers anchoring or the attachment of partially injured muscle fibers and thus contributes to localized muscle fibers regeneration.

This interplay between hydrogel pores, newly formed myofibers and preserved muscle fibers, results in a well-organized muscle tissue, displaying elongated myofibers emanating from the interface zone. Of note, this bundling myofibers organization at the vicinity of the hydrogel was not found in the empty defect control (Figure 6(f)). These results highlight that our acellular strategy sustains the attachment of the remaining injured tissue with the hydrogel and creates neo-regenerated/repaired area that promotes the sealing of these two matrices. In the context of muscle regeneration, the detailed contribution of the local formation of newly muscle fibers at the interface between remaining muscle tissue and the EPH remains to be determined.

In this study, we demonstrated that DGL/PEG effervescent porous hydrogels (EPH) serve as a suitable substrate for the formation of contractile myotubes *in vitro*, a crucial factor for efficient muscle recovery. Our EPH provides an appropriate structural environment, as well as biochemical and mechanical cues necessary for the proliferation and differentiation of muscle cells. Leveraging their biocompatibility, injectability, porosity, and versatile mechanical and swelling properties, we explored the potential of EPH as a supportive structure for repairing and regenerating muscle defects using rat models. While EPH effectively filled defects and underwent rapid cellularization and vascularization, our initial hypothesis that they would directly support the formation of myotubes and myofibers within their pores was not confirmed *in vivo*. Rather, our experiments revealed that it acted as a guiding structure, contributing to the organized formation of muscle at its periphery. One limitation of our study is the absence of functional measurements, which could provide useful insights into the balance between scar remodeling, myofiber regeneration, and hydrogel degradation. Further studies should be conducted to precisely characterize the functional outcomes of the EPH on muscle regeneration after VML injury. Although EPH remains a promising biomaterial for addressing current challenges associated with muscle injuries due to its injectability, further experiments are necessary to gain a more comprehensive understanding of EPH's role within the inflammatory reaction and its impact on the functionality of regenerated muscle, particularly in more relevant VML models.

Acknowledgements

We thank the CIQLE and SCAR platforms (SFR Santé Lyon-Est, UAR3453 CNRS, US7 Inserm, UCBL) for image acquisitions and animal experiments, and Novotec (France) for immunohistochemical and immunofluorescence staining. Financial support from the IR INFRANALYTICS FR2054 for conducting the research is gratefully acknowledged.

Author contributions

Conceptualization: LG, JS, and VG; data curation: JS and VG; formal Analysis: LG, MB, CP, JS, and VG; funding acquisition: JS and VG; investigation: LG, MB, EC, CP, JS, and VG; methodology: LG, MB, EC, JS,VG; project administration: JS and VG; resources: TL, JS, and VG; supervision: JS and VG; validation: JS and VG; visualization: LG, MB,CP, JS, and VG; writing—original draft: LG, JS, and VG; writing—review & editing: LG, MB, TL, JS, and VG. All authors have read and agreed to the published version of the manuscript.

Declaration of conflicting interests

The author(s) declared no potential conflicts of interest with respect to the research, authorship, and/or publication of this article.

Funding

The author(s) disclosed receipt of the following financial support for the research, authorship, and/or publication of this article: Agence Nationale de la Recherche (grant number ANR-17-CE19-0009), the "Association Française contre les Myopathies" (AFM) under the MyoNeurALP Alliance grant and the Fondation pour la Recherche Médicale (PBR202206016093).

ORCID iD

Vincent Gache https://orcid.org/0000-0002-2928-791X

Supplemental material

Supplemental material for this article is available online.

References

1. Janssen IA N, Heymsfield SB, Wang ZM, et al. Skeletal muscle mass and distribution in 468 men and women aged 18–88 yr. *J Appl Physiol* 2000; 89: 81–88.
2. Sluka KA. *Gray's anatomy - The anatomical basis of clinical practice* (Chap. 5). Elsevier, 2016.
3. Frontera WR and Ochala J. Skeletal muscle a brief review of structure and function. *Calcif Tissue Int* 2015; 96: 183–195.
4. Turner NJ and Badylak S F. Regeneration of skeletal muscle. *Cell Tissue Res* 2012; 347: 759–774.
5. Yin H, Price F and Rudnicki MA. Satellite cells and the muscle stem cell niche. *Physiol Rev* 2013; 93: 23–67.
6. Corona BT, Rivera JC, Owens JG, et al. Volumetric muscle loss leads to permanent disability following extremity trauma. *J Rehabil Res Dev* 2015; 52: 785–792.
7. Quarta M, Cromie M, Chacon R, et al. Bioengineered constructs combined with exercise enhance stem cell-mediated treatment of volumetric muscle loss. *Nat Commun* 2017; 8: 1–17.
8. Larouche JA, Fraczek PM, Kurpiers SJ, et al. Neutrophil and natural killer cell imbalances prevent muscle stem cell-mediated regeneration following murine volumetric muscle loss. *Proc Natl Acad Sci USA* 2022; 119: 1–12.

9. Gilbert-Honick J and Grayson W. Vascularized and innervated skeletal muscle tissue engineering. *Adv Heal Mater* 2020; 9: 248–256.
10. Vekris MD, Beris AE, Lykissas MG, et al. Restoration of elbow function in severe brachial plexus paralysis via muscle transfers. *Injury* 2008; 39: 15–22.
11. Tu YK, Yen CY, Ma CH, et al. Soft-tissue injury management and flap reconstruction for mangled lower extremities. *Injury* 2008; 39: 75–95.
12. Lee KT and Mun GH. A systematic review of functional donor-site morbidity after latissimus dorsi muscle transfer. *Plast Reconstr Surg* 2014; 134: 303–314.
13. Eugenis I, Wu D and Rando TA. Cells, scaffolds, and bioactive factors: Engineering strategies for improving regeneration following volumetric muscle loss. *Biomaterials* 2021; 278: 121173.
14. Langridge B, Griffin M and Butler PE. Regenerative medicine for skeletal muscle loss: a review of current tissue engineering approaches. *J Mater Sci Mater Med* 2021; 32: 1–16.
15. Corona BT and Greising SM. Challenges to acellular biological scaffold mediated skeletal muscle tissue regeneration. *Biomaterials* 2016; 104: 238–246.
16. Hernandez JL and Woodrow KA. Medical applications of porous biomaterials: features of porosity and tissue-specific implications for biocompatibility. *Adv Healthc Mater* 2022; 11: 1–50.
17. Chen S, Nakamoto T, Kawazoe N, et al. Engineering multilayered skeletal muscle tissue by using 3D microgrooved collagen scaffolds. *Biomaterials* 2015; 73: 23–31.
18. Kim M, Kim W and Kim G. Topologically micropatterned collagen and poly(ϵ-caprolactone) struts fabricated using the poly(vinyl alcohol) fibrillation/leaching process to develop efficiently engineered skeletal muscle tissue. *ACS Appl Mater Interfaces* 2017; 9: 43459–43469.
19. Gattazzo F, De Maria C, Rimessi A, et al. Gelatin–genipin-based biomaterials for skeletal muscle tissue engineering. *J Biomed Mater Res Part B Appl Biomater* 2018; 106: 2763–2777.
20. Jana S, Cooper A and Zhang M. Chitosan scaffolds with unidirectional microtubular pores for large skeletal myotube generation. *Adv Healthc Mater* 2013; 2: 557–561.
21. Kroehne V, Heschel I, Schügner F, et al. Use of a novel collagen matrix with oriented pore structure for muscle cell differentiation in cell culture and in grafts. *J Cell Mol Med* 2008; 12: 1640–1648.
22. Griveau L, Lafont M, Le Goff H, et al. Design and characterization of an *in vivo* injectable hydrogel with effervescently generated porosity for regenerative medicine applications. *Acta Biomater* 2022; 140: 324–337.
23. Tanner GI, Schiltz L, Narra N, et al. Granular hydrogels improve myogenic invasion and repair after volumetric muscle loss. *Adv Healthc Mater* 2024: e2303576.
24. Boonen KJM, Rosaria-Chak KY, Baaijens FPT, et al. Essential environmental cues from the satellite cell niche: optimizing proliferation and differentiation. *Am J Physiol Cell Physiol* 2009; 296: 1338–1345.
25. Chen CL, Wei SY, Chen WL, et al. Reconstructing vascular networks promotes the repair of skeletal muscle following volumetric muscle loss by pre-vascularized tissue constructs *J Tissue Eng* 2023; 14: 20417314231201231.
26. Carrancá M, Griveau L, Remoué N, et al. Versatile lysine dendrigrafts and polyethylene glycol hydrogels with inherent biological properties: *in vitro* cell behavior modulation and *in vivo* biocompatibility. *J Biomed Mater Res Part A* 2021; 109: 926–937.
27. Laumonier T, Koenig S, Saüc S, et al. Isolation of human myoblasts, assessment of myogenic differentiation, and store-operated calcium entry measurement. *J Vis Exp* 2017; 2017: 1–9.
28. Wu X, Corona BT, Chen X, et al. A standardized rat model of volumetric muscle loss injury for the development of tissue engineering therapies. *Biores Open Access* 2012; 1: 280–290.
29. Schneider CA, Rasband WS and Eliceiri KW. NIH Image to ImageJ: 25 years of image analysis. *Nat Methods* 2012; 9: 671–675.
30. Sahu M, Reddy VR, Kim B, et al. Fabrication of Cu_2ZnSnS_4 light absorber using a cost-effective mechanochemical method for photovoltaic applications. *Materials* 2022; 15: 1–16.
31. Chieng BW, Ibrahim NA, Yunus WMZW, et al. Poly(lactic acid)/poly(ethylene glycol) polymer nanocomposites: Effects of graphene nanoplatelets. *Polymers* 2014; 6: 93–104.
32. Couturaud B, Bondia AM, Faye C, et al. Grafting of poly-L-lysine dendrigrafts onto polypropylene surface using plasma activation for ATP immobilization – nanomaterial for potential applications in biotechnology. *J Colloid Interface Sci* 2013; 408: 242–251.
33. Scholl M, Nguyen TQ, Bruchmann B, et al. The thermal polymerization of amino acids revisited; Synthesis and structural characterization of hyperbranched polymers from L-lysine. *J Polym Sci Part A Polym Chem* 2007; 45: 5494–5508.
34. Kunimoto K, Sasaki C, Kuwae A, et al. Characterization of microbial poly (ε-l-lysine) by FT-IR, Raman and solid state 13C NMR spectroscopies. *J Mol Struct* 2003; 655: 149–155.
35. Nazarpoor Z, Ma S, Fanson PT, Alexeev OS, et al. Decomposition of poly(amidoamine) (PAMAM) dendrimers under O_2 plasma conditions. *Polym Degrad Stab* 2012; 97: 439–451.
36. Asano A, Tanaka C and Murata Y. NMR determination of crystallinity for poly(ϵ-l-lysine) Author. *Polymer* 2007; 48: 3809–3816.
37. Collet H, Souaid E, Cottet H, et al. An Expeditious multigram-scale synthesis of lysine dendrigraft (DGL) polymers by aqueous N-carboxyanhydride polycondensation. *Chemistry* 2010; 16: 2309–2316.
38. Huang R, Liu S, Shao K, et al. Evaluation and mechanism studies of PEGylated dendrigraft poly-L-lysines as novel gene delivery vectors. *Nanotechnology* 2010; 21: 265101.
39. Puskas JE, Seo KS and Sen MY. Green polymer chemistry: precision synthesis of novel multifunctional poly(ethylene glycol)s using enzymatic catalysis. *Eur Polym J* 2011; 47: 524–534.
40. Engler AJ, Griffin MA, Sen S, et al. Myotubes differentiate optimally on substrates with tissue-like stiffness : pathological implications for soft or stiff microenvironments. *J Cell Biol* 2004; 166: 877–887.

41. Andrés V and Walsh K. Myogenin expression, cell cycle withdrawal, and phenotypic differentiation are temporally separable events that precede cell fusion upon myogenesis. *J Cell Biol* 1996; 132: 657–666.
42. Schiaffino S, Rossi AC, Smerdu V, et al. Developmental myosins: expression patterns and functional significance. *Skelet Muscle* 2015; 5: 1–14.
43. Benton G, Arnaoutova I, George J, et al. Matrigel: from discovery and ECM mimicry to assays and models for cancer research. *Adv Drug Deliv Rev* 2014; 79: 3–18.
44. Ferri-Angulo D, Yousefi-Mashouf H, Michel M, et al. Versatile fiber-reinforced hydrogels to mimic the microstructure and mechanics of human vocal-fold upper layers. *Acta Biomater* 2023; 172: 92–105.
45. Laumonier T and Menetrey J. Muscle injuries and strategies for improving their repair. *J Exp Orthop* 2016; 3: 15.
46. Mih JD, Marinkovic A, Liu F, et al. Matrix stiffness reverses the effect of actomyosin tension on cell proliferation. *J. Cell Sci* 2012; 125: 5974–5983.
47. Francoia JP, Rossi JC, Monard G, et al. Digitizing poly-L-lysine dendrigrafts: from experimental data to molecular dynamics simulations. *J Chem Inf Model* 2017; 57: 2173–2180.
48. De Pascalis C and Etienne-Manneville S. Single and collective cell migration: the mechanics of adhesions. *Mol Biol Cell* 2017; 28: 1833–1846.
49. Lan MA, Gersbach CA, Michael KE, et al. Myoblast proliferation and differentiation on fibronectin-coated self assembled monolayers presenting different surface chemistries. *Biomaterials* 2005; 26: 4523–4531.
50. Ziemkiewicz N, Talovic M, Madsen J, et al. Laminin-111 functionalized polyethylene glycol hydrogels support myogenic activity *in vitro*. *Biomed Mater* 2018; 13: 65007.
51. Fuoco C, Sangalli E, Vono R, et al. 3D hydrogel environment rejuvenates aged pericytes for skeletal muscle tissue engineering. *Front Physiol* 2014; 5: 203.
52. Velasco-Mallorquí F, Fernández-Costa JM, Neves L, et al. New volumetric CNT-doped gelatin-cellulose scaffolds for skeletal muscle tissue engineering. *Nanoscale Adv* 2020; 2: 2885–2896.
53. Poveda-Reyes S, Moulisova V, Sanmartín-Masiá E, et al. Gelatin—hyaluronic acid hydrogels with tuned stiffness to counterbalance cellular forces and promote cell differentiation. *Macromol Biosci* 2016; 16(9): 1311–1324.
54. Shansky J, Chromiak J, Tatto M, et al. A simplified method for tissue engineering skeletal muscle organoids *in vitro*. *Vitr Cell Dev BiolAnim* 1997; 33: 659–661.
55. Kaufman CD, Liu SC, Cvetkovic C, et al. Emergence of functional neuromuscular junctions in an engineered, multicellular spinal cord-muscle bioactuator. *APL Bioeng* 2020; 4(2): 026104.
56. Labruyere C, Noailles T, Steltzen C, et al. Anatomie moderne du ligament croisé antérieur – un seul faisceau plat torsadé élastographie . Comparaison d ' une population témoin et de sujets souffrant de tendinopathie patellaire. *Rev Chir Orthopédique Traumatol* 2015; 10: S250–S251.
57. Eggermont LJ, Rogers Z J, Colombani T, et al. Injectable cryogels for biomedical applications. *Trends Biotechnol* 2020; 38: 418–431.
58. Shi M, Bai L, Xu M, et al. Magnetically induced anisotropic conductive in situ hydrogel for skeletal muscle regeneration by promoting cell alignment and myogenic differentiation. *Chem Eng J* 2024; 484: 149019.
59. Ishibashi J, Perry RL, Asakura A, et al. MyoD induces myogenic differentiation through cooperation of its NH_2- and COOH-terminal regions. *J Cell Biol* 2005; 171: 471–482.
60. Cooper RN, Tajbakhsh S, Mouly V, et al. *In vivo* satellite cell activation via Myf5 and MyoD in regenerating mouse skeletal muscle. *J Cell Sci* 1999; 112: 2895–2901.
61. Zhang H, Wen J, Bigot A, et al. Human myotube formation is determined by MyoD–Myomixer/Myomaker axis. *Sci Adv* 2020; 6: 1–13.
62. Hernández-Hernández JM, García-González EG, Brun CE, et al. The myogenic regulatory factors, determinants of muscle development, cell identity and regeneration. *Semin Cell Dev Biol* 2017; 72: 10–18.
63. Feng LT, Chen ZN and Bian H. Skeletal muscle: molecular structure, myogenesis, biological functions, and diseases. *MedComm* 2024; 5: 1–25.
64. Mansour A, Romani M, Acharya AB, et al. Drug delivery systems in regenerative medicine: an updated review. *Pharmaceutics* 2023; 15: 1–23.
65. Xu X, Zheng L, Yuan Q, et al. Transforming growth factor-β in stem cells and tissue homeostasis. *Bone Res* 2018; 6: 2.
66. von Maltzahn J, Chang NC, Bentzinger CF, et al. Wnt signaling in myogenesis. *Trends Cell Biol* 2012; 22: 602–609.
67. Shi M, Dong R, Hu J, et al. Conductive self-healing biodegradable hydrogel based on hyaluronic acid-grafted-polyaniline as cell recruitment niches and cell delivery carrier for myogenic differentiation and skeletal muscle regeneration. *Chem Eng J* 2023; 457: 141110.
68. Chamieh J, Biron JP, Cipelletti L, et al. Monitoring biopolymer degradation by Taylor dispersion analysis. *Biomacromolecules* 2015; 16: 3945–3951.
69. Larouche J. Robust inflammatory and fibrotic signaling following volumetric muscle loss : a barrier to muscle regeneration. *Cell Death Dis* 2018; 9: 18–20.
70. Aguilar CA, Greising SM, Watts A, et al. Multiscale analysis of a regenerative therapy for treatment of volumetric muscle loss injury. *Cell Death Discov* 2018; 4: 33.
71. Trindade MCD, Lind M, Sun D, et al. *In vitro* reaction to orthopaedic biomaterials by macrophages and lymphocytes isolated from patients undergoing revision surgery. *Biomaterials* 2001; 22: 253–259.
72. Sadtler K, Estrellas K, Allen BW, et al. Developing a pro-regenerative biomaterial scaffold microenvironment requires T helper 2 cells. *Science* 2016; 352(6283): 366–370.
73. Schiltz L, Grivetti E, Tanner GI, et al. Recent advances in implantable biomaterials for the treatment of volumetric muscle loss. *Cells Tissues Organs* Epub ahead of print 12 January 2024; 1–17.
74. Aurora A, Roe JL, Corona BT, et al. An acellular biologic scaffold does not regenerate appreciable de novo muscle tissue in rat models of volumetric muscle loss injury. *Biomaterials* 2015; 67: 393–407.